Draft version August 27, 2019
Typeset using LaTeX **twocolumn** style in AASTeX62

SOAR TESS Survey. I: Sculpting of TESS planetary systems by stellar companions

Carl Ziegler,[1] Andrei Tokovinin,[2] César Briceño,[2] James Mang,[3] Nicholas Law,[4] and Andrew W. Mann[5]

[1] *Dunlap Institute for Astronomy and Astrophysics, University of Toronto, 50 St. George Street, Toronto, Ontario M5S 3H4, Canada*
[2] *Cerro Tololo Inter-American Observatory, Casilla 603, La Serena, Chile*
[3] *University of California, Berkeley, 510 Campbell Hall, Astronomy Department, Berkeley, CA 94720, USA*
[4] *Department of Physics and Astronomy, University of North Carolina at Chapel Hill, Chapel Hill, NC 27599-3255, USA*
[5] *Department of Physics and Astronomy, The University of North Carolina at Chapel Hill, Chapel Hill, NC 27599-3255, USA*

ABSTRACT

TESS is finding transiting planet candidates around bright, nearby stars across the entire sky. The large field-of-view, however, results in low spatial resolution, therefore multiple stars contribute to almost every TESS light curve. High-angular resolution imaging can detect the previously unknown companions to planetary candidate hosts that dilute the transit depths, lead to host star ambiguity, and in some cases are the source of false-positive transit signals. We use speckle imaging on SOAR to search for companions to 542 TESS planet candidate hosts in the Southern sky. We provide correction factors for the 117 systems with resolved multiples due to the photometric contamination from the additional sources. The contamination in TESS due to close binaries is similar to that found in surveys of *Kepler* planet candidates. For the solar-type population, we find a deep deficit of close binary systems with projected stellar separations less than 100 AU among planet candidate hosts (44 observed binaries compared to 125 expected based on field binary statistics). The close binary suppression among TESS planet candidate hosts is similar to that seen for the more distant *Kepler* population. We also find a large surplus of the TESS planet candidates in wide binary systems, detected in both SOAR and *Gaia* DR2 (119 observed binaries compared to 77 expected). These wide binaries host almost exclusively giant planets, however, suggesting orbital migration, caused by perturbations from the stellar companion, may lead to planet-planet scattering and suppress the population of small planets in wide binaries. Both trends are also apparent in the M-dwarf planet candidate hosts.

1. INTRODUCTION

Over a decade-long primary and extended missions, the *Kepler* telescope (Borucki et al. 2010) detected the majority of known exoplanets. *Kepler* probed the large (Howard et al. 2012) and diverse (Lissauer et al. 2011; Welsh et al. 2012) Galactic population of planetary systems, but only looked at relatively small regions of the sky at a time. Also, the observed stars in the prime mission were generally too distant for precision follow-up observations.

Beginning in 2018 July, the Transiting Exoplanet Survey Satellite (TESS, Ricker et al. 2014) searched the Southern sky for exoplanets around nearby stars. These typically bright targets are accessible to measurements of planet masses with precision radial velocity and atmospheric characterization of planets with transmission spectroscopy. Several planets around bright stars have been confirmed (Huang et al. 2018; Dragomir et al. 2019; Vanderburg et al. 2019), with hundreds of additional candidates awaiting follow-up observations.[1]

The simultaneous field-of-view required for TESS is large, approximately 6% of the entire sky, which it covers with a relatively coarse pixel scale of $21''$ px^{-1}. For reference, each TESS pixel subtends a region of the sky approximately 25× that of each *Kepler* pixel. Each TESS pixel observes the flux made up of the blended contributions of multiple sources. The TESS Input Catalog (TIC, Stassun et al. 2018, 2019) determined the contamination from known point sources in two catalogs (APASS and 2MASS) likely to be in the TESS aperture for 3.8 million stars. While these catalogs limiting magnitudes are relatively faint compared to the typically bright TESS targets ($T_{mag,limiting}$ ∼17-19), they are based on seeing-limited observations and are not sensitive to binaries with separations less than 1-2$''$. Like-

Corresponding author: Carl Ziegler
carl.ziegler@dunlap.utoronto.ca

[1] https://tess.mit.edu/alerts/

wise, Gaia DR2 generally does not recover binaries with separations of less than $\sim 0\farcs7$, in particular for bright stars (Ziegler et al. 2018a).

High-resolution imaging has proven to be critical to confirm and characterize transiting planet candidates. Half of solar-type stars (Raghavan et al. 2010) and a quarter of M-dwarfs (Winters et al. 2019) are found in multiple systems. The maximum of the distribution of orbital separations ($\sim$50 AU for a solar-type binary and 20 AU for M-dwarfs), at a typical distance to a TESS host star of approximately 100 pc, peaks at angular separations of $0\farcs2$ to $0\farcs5$, accessible only by high angular resolution imaging. Therefore, most contamination from binary systems is not accounted for in the TIC.

For *Kepler*, the planet radius estimates for stars with detected companions increased by a factor of 1.6 on average (Ciardi et al. 2015; Ziegler et al. 2018b). In many cases, the identity of the planetary host star may be ambiguous, leading to two different possible radius estimates based on either scenario. In addition, the absence of companions can be used to rule out many common false positive scenarios, allowing planets to be statistically validated (Morton & Johnson 2011).

The number of planet candidates detected by *Kepler* and currently by TESS outstrips the resources available on conventional high-resolution instruments, such as laser-guide star adaptive optics.[2] A useful strategy with *Kepler* was to perform a broad survey with a visible-light high-resolution instrument on a moderately sized telescope. These observations are able to find the majority of both physically bound companions and low-contrast asterisms that significantly alter the radius estimate of the planet candidate. The Robo-AO *Kepler* survey (Law et al. 2014; Baranec et al. 2016; Ziegler et al. 2017) observed 3857 planet candidate host stars with a laser-assisted adaptive optics (AO) robotic instrument on a 2-m class telescope (Baranec et al. 2014). The discoveries of companions corrected the radius estimates for 814 planet candidates (Ziegler et al. 2018b), contributed to the validation of over a thousand *Kepler* planets (Morton et al. 2016), and informed future observations with large-aperture telescopes. Six years after the *Kepler* prime mission ended, over half of the *Kepler* planet candidates have only been imaged at high-resolution by Robo-AO.

The TESS sample can largely be covered by speckle interferometry, due to host stars that are on average several magnitudes brighter than *Kepler*. Speckle interferometry on SOAR has been developed and optimized over the past decade, and at present can image up to 300 targets a night with diffraction-limited resolution (Tokovinin 2018). Mann et al. (2019) found the astrometric precision of SOAR speckle imaging to be among the best compared to similar non-fixed high-resolution instruments. Imaging in Cousins-I band, at the center of the TESS bandpass, the dilution in the TESS light curves due to detected companions can be accurately determined to correct radius estimates.

Theory suggests the presence of a nearby stellar companion can have a dire impact on the formation of circumstellar planetary systems: stirring planetesimals (Quintana et al. 2007), perturbing orbits resulting in high eccentricity tidal migration (Naoz et al. 2012), truncating protoplanetary discs and shortening their lifetime (Jang-Condell et al. 2008; Kraus et al. 2012), and increasing photoevaporation (Alexander 2012). Ngo et al. (2016) found that hot Jupiters have significantly fewer companions at close separations compared to field stars, but many more at wider separations. This suggests these hot Jupiters may have been driven inwards to their present few-day orbits by perturbations from the companion stars. Bolstering this interpretation, the Robo-AO *Kepler* survey found that hot Jupiters were significantly more likely to be found in binary systems than other types of planets (Ziegler et al. 2018c). Deacon et al. (2016), however, found no difference in the wide ($\rho > 3000AU$) binary rate between transiting planet hosts and field stars in the *Kepler* field.

Kraus et al. (2016), observing 382 *Kepler* planet candidates with adaptive optics on Keck, found a dearth of *Kepler* planets in close binary systems. This deficit was modeled as a binary suppression factor of 0.34 at separations below approximately 47 AU. Extrapolating this out suggests that one-fifth of the solar-type stars in the galaxy can not host planets due to the influence of a stellar companion. It is unclear, however, if the survival of planets in close binary systems is random, or a result of other factors, such as the binary eccentricity or the mutual inclination to the planetary system of the binary system. The detection image provides only an instantaneous projected separation, s. Further monitoring is needed to determine the true orbital parameters that could provide insight into how some planetary systems form and survive in this harsh environment.

The TESS planet candidate hosts are relatively nearby; on average, less than half the distance as the *Kepler* hosts, based on the TIC distance estimates (Stassun et al. 2019). The 4.1m SOAR telescope can, therefore, detect companions at solar-system separations (s=10-50 AU) to the vast majority of TESS targets. Evidence of

[2] For example, the acquisition time of Keck-AO averages 9 minutes (Wizinowich et al. 2006), so over a hundred nights would be needed to observe the *Kepler* planet candidates.

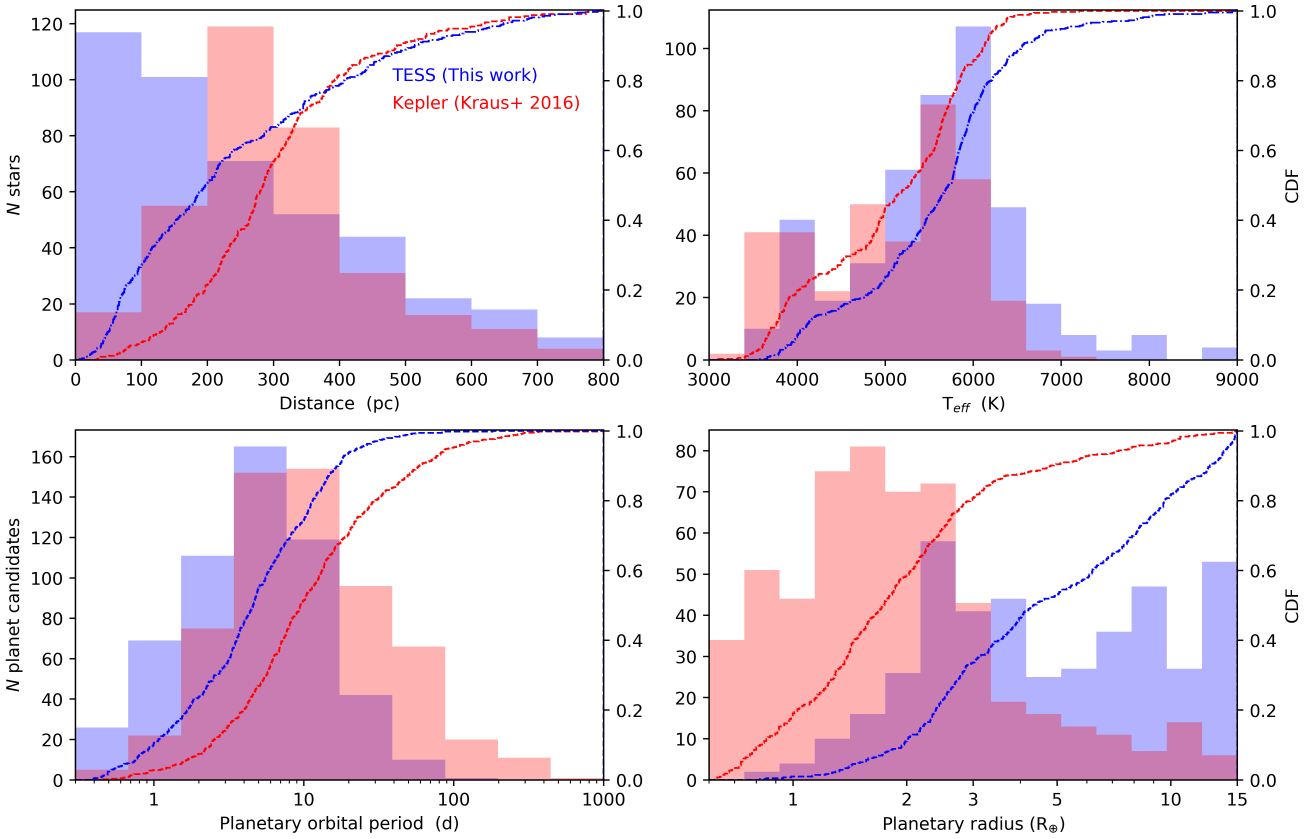

Figure 1. The properties of the 542 TESS planet candidate hosts observed by SOAR in this survey, presented as a binned histogram with an overplotted cumulative density function. For comparison, the properties of the 382 *Kepler* planet candidate hosts observed in Kraus et al. (2016) are also plotted. In general, the TESS planets are closer to the solar system, have slightly hotter hosts, orbit with shorter periods, and are larger than the *Kepler* planets targeted by the Kraus et al. (2016) survey.

suppression in the binary rate for TESS planet candidates in this regime would serve both as an independent validation of the ruinous effect binaries have on planetary systems, and, since the TESS planets are spread over the entire sky, confirmation of the effect in a more representative sample of the Galactic planetary population. Indeed, Matson et al. (2018) did not detect binary suppression in a sample of K2 stars, which are spread in fields across the ecliptic plane. The authors note the non-detection is tenuous, however, and more high-resolution observations of exoplanet hosts are needed.

We begin in Section 2 by detailing our observations and data analysis. We present the results of the survey in Section 3, and explore the impact binaries have on the TESS planets in Section 4. We discuss the results further in Section 5. Finally, we conclude in Section 6.

2. OBSERVATIONS AND ANALYSIS

2.1. *Target selection*

The hosts of TESS planet candidates (TESS objects of interest, or TOIs) were selected from the data releases available online at the TESS data release portal.[3] Faint stars (typically, T_{mag} <13 mag) that are not well suited for speckle observations were not targeted; this limit reduces the number of late-type stars that are observed in this survey. Previously confirmed planet hosts, primarily from the WASP (Street et al. 2003) and HATS (Bakos 2018) surveys, were excluded from the target selection as these systems have been heavily studied in the past (e.g., Ngo et al. 2015; Evans et al. 2016, 2018). Seventeen community detected TESS planet candidates[4] were also observed but were not used in the subsequent analysis in this work. To increase observing efficiency, target acquisition was improved using precise target coordinates, determined for each night with proper motions from Gaia DR2 (Gaia Collaboration et al. 2018), when available, and from the TIC (Stassun et al. 2019) otherwise. As previously noted in Arenou et al. (2018), we

[3] https://tev.mit.edu/toi/, account required for access.

[4] From CTOI list, available at https://exofop.ipac.caltech.edu/tess/view_ctoi.php

find that many targets with only two-parameter astrometric solutions in Gaia DR2 are actually close binaries.

The properties of the host stars and planet candidates observed are plotted in Figure 1.

2.2. *SOAR observations and data reduction*

We observed 542 TESS planet candidate hosts with the high-resolution camera (HRCam) imager on the 4.1-m Southern Astrophysical Research (SOAR) telescope over seven nights in 2018-2019. The observation procedure and data reduction are described in Tokovinin (2018). Briefly, each observation consists of 400 frames, typically consisting of a 200×200 binned pixels region of interest centered on the target star (6.″3 on a side at the pixel scale of 0.″01575 and 2×2 binning), taken in approximately 11 s with an Andor iXon-888 camera. The resulting data cube is processed by a custom IDL script, which computes the power spectrum, in which a resolved multiple stellar system will appear as characteristic fringes. Binary parameters (separation, position angle, and magnitude difference) are determined from modeling the power spectrum. Secondary stars will appear as mirrored peaks in the speckle auto-correlation function (ACF), the Fourier transform of the power spectrum, at the separation and position angle of the companion. A shift-and-added image, centered on the brightest pixel in each frame, can remove the ambiguity in the position angle in many cases. Observations were taken in the I-band (λ_{cen}=824 nm, $\Delta\lambda$=170 nm), which is approximately centered on the TESS bandpass. Four resolved systems (TOI-123, 131, 138, and 146) were also imaged in V-band in preparation for a future association analysis. The detection limits are estimated from the fluctuations of the ACF computed in annular zones of increasing radii and verified by simulating binary companions to single stars from this program and "detecting" them. The exact pixel scale and detector orientation are determined for each run from a set of wide calibration binaries.

We detail the observations in Table 5 in the Appendix. The cumulative detection sensitivities are plotted in Figure 2.

2.3. *Planet radius corrections*

The additional flux from a nearby star will dilute the transit depth in the TESS light curves, resulting in an underestimated radius for the planet candidate. We compute correction factors to the radius estimates derived from the TESS light curves for two scenarios: 1) the planet orbits the target star; and 2) the planet orbits the secondary star which is bound to the primary star[5].

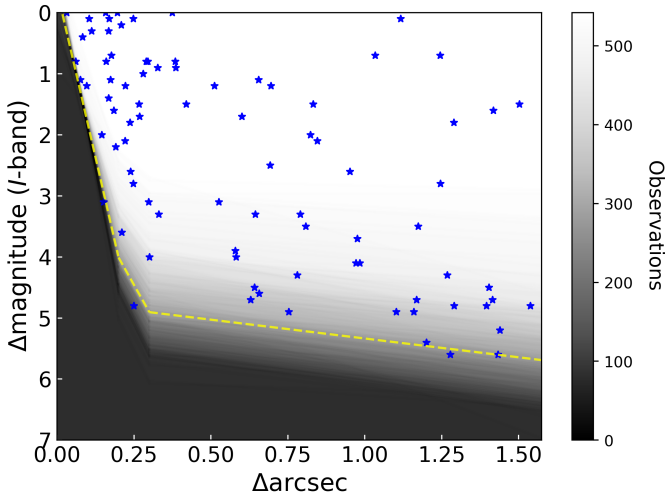

Figure 2. Close companions (ρ <1.″55) to TESS planet candidate hosts detected by SOAR speckle imaging, in terms of their I-band magnitude difference and separation from the primary star. The average detection limits of the observations are plotted, trending from black (no observations are sensitive to binaries with that combination of separation and contrast) to white (all 542 observations are sensitive to that combination). The yellow dashed line shows the median sensitivity for the survey.

For the first scenario, we use the relation from Law et al. (2014) to derive a radius correction factor,

$$X_{prim} = \frac{R_{p,A}}{R_{p,0}} = \sqrt{\frac{1}{F_A}} \quad (1)$$

where $R_{p,A}$ is the corrected radius of the planet orbiting the primary star, $R_{p,0}$ is the original planetary radius estimate based on the diluted transit signal, and F_A is the fraction of flux within the aperture from the primary star.

For the case where the planet candidate is bound to the secondary star, we use the relation for the radius correction factor,

$$X_{sec} = \frac{R_{p,B}}{R_{p,0}} = \frac{R_B}{R_A}\sqrt{\frac{1}{F_B}} \quad (2)$$

where $R_{p,B}$ is the corrected radius of the planet orbiting the secondary star bound to the primary star, R_B and R_A are the stellar radii of the secondary and primary

[5] A third scenario, in which the secondary star is unbound to the primary star, is unconstrained without color information. In future papers, we will use multi-band speckle imaging with SOAR to extend our analysis to the unbound scenario.

star, respectively, and F_B is the fraction of flux within the aperture from the secondary star.

We use the stellar radius estimates from the TIC (Stassun et al. 2019) when available for the primary stars. The radii of secondary companions in the scenario where they are bound to the target star were estimated using the observed contrast ratio in the *TESS* band (approximated using the I bandpass of SOAR) and finding the radius of an appropriately fainter star within the Dartmouth stellar models (Dotter et al. 2008).

The TIC includes a contamination ratio which takes into account stars within 10 TESS pixels of the target. This includes stars typically down to the limiting magnitude of the 2MASS (Skrutskie et al. 2006) and APASS (Henden et al. 2009) catalogs ($T \sim 17-19$). Using the list of detected close binaries to *TESS* planet candidate hosts and their binary parameters, a custom Python script crossmatched each of their coordinates to stars in the TIC catalog. We find 31 stars in the TIC had similar positions relative to the primary as was found in SOAR imaging ($\Delta\rho < 0\farcs5$ and $\Delta\theta$ <20°, or $[\Delta\theta \pm 180^o]$ <20°). The properties of these systems are available in Table 2 in the Appendix. One notable resolved binary in our survey is the pair TOI-658 and TOI-659. The magnitude differences in the TESS bandpass for wide binaries in the TIC are generally similar to that measured from the SOAR observations, supporting our use of I-band observations as a proxy for the TESS observations. A similar crossmatch was performed with Gaia DR2 (Gaia Collaboration et al. 2018), yielding 38 matches to SOAR detected companions. These companions were all widely separated ($\rho > 1''$). The separations measured by SOAR have a mean and median difference of 15 and 6 mas, respectively, compared to those reported in Gaia DR2. The average difference in magnitude differences between SOAR and Gaia DR2 is 0.16 mags, and is likely due to the different passbands. The properties of these systems are available in Table 3 in the Appendix.

We provide a correction factor for hosts, as in some cases the crossmatch between the TIC and the SOAR binary is ambiguous, however, we caution that the correction should be used judiciously. For all other systems, the contamination ratios reported should be used in addition to the TIC contamination ratio. In practice, the reported radius estimates of TESS planet candidates on the TESS data release portal and ExoFOP typically takes into account flux contamination. The additional correction due to binaries detected by SOAR is the product of the original radius estimate and the radius correction factor reported in this work.

2.4. *Physical association of companions*

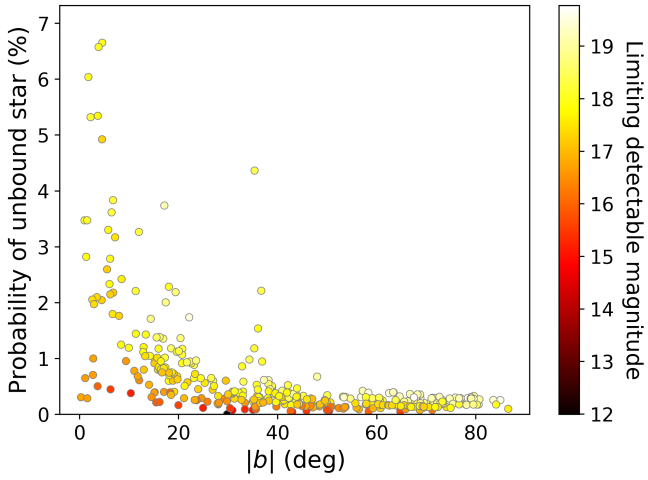

Figure 3. The probability of an unbound star being detected with the search radius of each observed TESS planet candidate as a function of Galactic latitude, based on *Gaia* DR2 stellar counts. Each target is colored by the limiting magnitude of detectable nearby stars in the SOAR speckle observations. We expect approximately three unbound stars in total to be detected near the TESS planet candidates.

A relatively large number of companions detected near *Kepler* planet candidates were unassociated, especially at separations greater than 1″ (Horch et al. 2014; Ziegler et al. 2018c). The TESS targets are spread across the sky, in regions of low and high stellar density, but generally at higher Galactic latitudes than the *Kepler* field. In addition, the targets are typically bright (T_{mag} <12 mag), and subsequently the detectable stars near them are several magnitude brighter than the *Kepler* stars, given approximately equal contrast sensitivity. It is likely then that the number of detected field stars will be reduced in the TESS sample.

We use the stellar densities in the region of sky around each target in Gaia DR2 Gaia Collaboration et al. (2018) to estimate the likelihood of a field star being detected near a TESS star. Gaia DR2 is essentially complete for sources down to G=17 mag, and down to G=19 mag in non-crowded fields (Gaia Collaboration et al. 2018). For our typical target with $I = 12$ mag and a contrast sensitivity of 5 mag, the faintest detectable companions will have $I \approx 17$ mag, comparable to the *Gaia* completeness limit.

For each target, we begin by performing a cone search in DR2 within 0.5°. We use the number of sources to determine the source density as a function of G magnitude. These stellar densities are combined with our detection sensitivity curves to estimate the number of field stars we can expect to find for that target (see Figure 3). Typically, targets near the galactic plane and near the

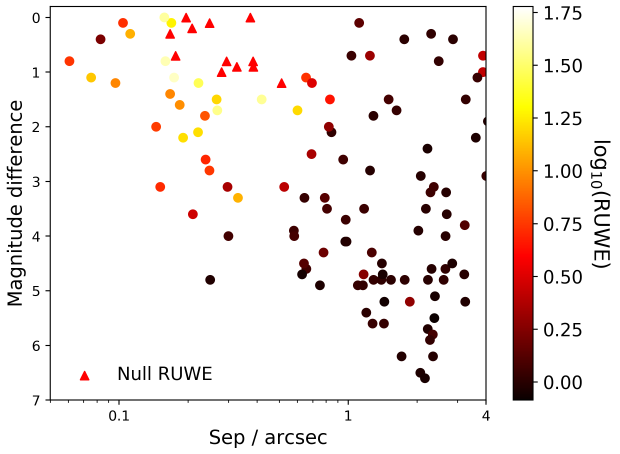

Figure 4. The properties of companions to TESS planet candidate hosts resolved by SOAR, colored by the logarithm of each system's Gaia DR2 RUWE value, a metric quantifying the quality of the Gaia astrometric solution. Companions in systems with null RUWE values are indicated by a red triangle. While Gaia does not resolve close binaries ($\rho < 0.''7$), the high or null RUWE value may be used to infer the existence of a companion star. This method is successful with an accuracy of 86% in our survey.

Small and Large Magellanic clouds are far more likely to have a field companion.

We perform a Monte Carlo analysis using these probabilities and the distribution of contrast sensitivity to simulate 10^4 surveys and find that on average, we should detect 3.2±0.5 field stars within $3.''15$ of the observed TESS targets. The field companions are nearly always high-contrast (with a large ΔI). We, therefore, expect the impact on the subsequent analysis due to unassociated asterisms of field stars to be negligible.

3. RESULTS

We detected 88 and 123 companions within $1.''5$ and $3''$ of 84 and 117 TESS planet candidate hosts, respectively, out of 542 observed with speckle imaging on SOAR. This implies a companion rate within $1.''5$ and $3''$ for TESS planet candidates of 16.2±1.7% and 22.7±2.0%, respectively. The properties of the detected companions are plotted in Figure 2, along with the average detection sensitivities from all observations which are detailed in Table 5 in the Appendix. We include the radius correction factors for planets in these systems, whether they orbit the primary or secondary star. The auto-correlation functions of resolved systems showing the position of the companions are shown in Figures 12-15 in the Appendix.

The results of each night's observations were processed within a week and posted on the TESS Exoplanet Follow-up Observing Program (ExoFOP) webpage[6] to aid in confirmation of the planet candidates. Several studies (Vanderburg et al. 2019; Rodriguez et al. 2019; Quinn et al. 2019; Espinoza et al. 2019; Jones et al. 2019) have used the SOAR speckle results to confirm early TESS planets.

Table 1. Nearby stars detected by SOAR to TESS planet candidate hosts

TOI	Separation ($''$)	P.A. (deg)	Contrast (I-band)	T_{eff} (K)	Distance (pc)	Proj. Sep.[a] (AU)	Radius correction factor (primary host)	(secondary host)	Prev. det.?	WDS DD
123	1.2894	294.6	1.8	6188	72	92	1.091	2.404	3	SEE443
128	2.2195	153.8	2.4	6086	67	148	1.053	3.13	2	FIN92
128	1.5337	40.3	5.1	6086	67	102	1.005	10.352	1	
131	0.0755	207.1	1.1	4174	55	4	1.168	1.932	1	
138	0.0964	257.0	1.2	5722	128	12	1.154	2.005	1	
141	1.1999	305.2	5.4	5795	48	57	1.003	10.881	1	
141	0.4429	239.5	4.9	5795	48	21	1.005	8.66	1	
146	0.2896	76.1	0.8	6905			1.216		1	
147	2.6583	217.6	4.6	5620	820	2179	1.007		3	
149	1.117	132.6	0.1	5914	376	419	1.383		3	TDS161
153	0.1691	173.6	0.1	6142	436	73	1.383	1.425	1	
159	0.6444	17.5	3.3	6979	333	214	1.024	4.594	1	
161	0.1961	101.2	0.0	5388	333	65	1.414	1.414	1	
165	2.4855	254.5	0.8	6038	193	479	1.216	1.686	2	RST164

[6] https://exofop.ipac.caltech.edu/tess/

Table 1 – *Continued*

TOI	Separation (″)	P.A. (deg)	Contrast (I-band)	T_{eff} (K)	Distance (pc)	Proj. Sep.[a] (AU)	Radius correction factor (primary host)	Radius correction factor (secondary host)	Prev. det.?	WDS DD
165	1.0169	131.3	5.2	6038	193	196	1.004	10.564	1	
167	0.1593	306.6	0.8	5551	293	46	1.216	1.776	3	
172	1.1021	319.1	4.9	5911	225	247	1.005	9.603	1	
180	1.2682	63.7	4.3	6082	270	342	1.009	7.197	3	
183	0.083	98.5	0.4	6270	200	16	1.301	1.495	1	
183	3.1806	302.0	5.1	6270	200	636	1.005	10.056	1	
187	0.8456	104.5	2.1	6725	177	149	1.07	2.797	1	
188	1.2904	5.8	4.8	6340	203	261	1.006	8.547	1	
189	0.9716	341.7	4.1	6054	177	171	1.011	6.411	1	
211	0.2083	258.3	0.2	5873	121	25	1.353	1.338	1	
224	0.0607	31.1	0.8	3689	64	3	1.216	1.63	1	
235	0.8326	291.6	1.5	5454	104	86	1.119	2.151	2	B2080
240	2.3656	197.6	3.1	4333	74	175	1.028	4.128	3	
242	0.8233	164.3	2.0	6083	589	484	1.076	2.66	1	
245	1.6268	258.2	1.7	6208	126	204	1.1	2.313	2	B584
252	0.4192	311.5	1.5	5071	190	79	1.119	2.105	1	
253	2.6623	351.2	4.0	4020	30	79	1.012	5.734	3	
258	2.0749	343.2	2.9	6474	561	1164	1.034	3.662	3	
264	0.6413	331.5	4.5	5773	422	270	1.008	7.22	1	
268	2.3025	51.2	0.3	5868	305	702	1.326	1.373	2	HU1368
293	0.7905	0.3	3.3	5817	313	247	1.024	4.22	1	
295	0.9838	151.8	4.1	5663	389	382	1.011	6.656	1	
308	0.1576	45.2	0.0	4416	201	31	1.414		1	
309	0.3266	77.9	0.9	5312	345	112	1.199	1.692	1	
322	0.1761	126.5	0.7	5868	277	48	1.235	1.537	1	
325	0.5815	222.2	4.0	4275	180	104	1.012		1	
337	0.1451	60.8	2.0	5369	292	42	1.076	2.606	1	
340	0.237	338.0	1.8	5655	497	117	1.091	2.39	1	
343	2.8471	321.0	4.5	5695	438	1247	1.008	7.817	3	
346	1.4329	285.3	5.6	5835	745	1067	1.003		1	
348	1.3959	40.8	4.8	5714	420	586	1.006	8.958	1	
364	0.3739	96.1	0.0	6219	265	99	1.414	1.414	1	
369	0.6949	139.4	1.2	6228	126	87	1.154		2	B600
372	0.2386	260.6	2.6	5400	340	81	1.045	3.334	1	
378	0.1839	330.0	1.6	5894	629	115	1.109	2.316	1	
378	3.3108	312.3	1.5	5894	629	2082	1.119	2.232	1	
379	0.031	28.8	0.0	5895	227	7	1.414	1.414	1	
383	0.2665	333.6	1.5	5951	204	54	1.119	2.118	1	
386	1.1739	274.4	3.5	8100	452	530	1.02	5.111	3	
387	2.2878	342.9	3.2	6191	193	441	1.026	4.306	3	
394	3.2284	220.2	3.8	6329	149	481	1.015	5.583	2	BU529
402	1.4388	233.4	5.2	5175	44	63	1.004	10.825	1	
405	0.3856	321.5	0.9	6138	266	102	1.199	1.785	1	
409	3.2443	20.4	5.2	4986	53	171	1.004	10.819	1	
415	2.2303	89.6	4.8	6471	381	849	1.006	8.547	1	
422	1.4038	118.8	4.5	5823	98	137	1.008	7.22	1	
427	2.6122	152.9	4.8	5409	145	378	1.006	8.843	1	

Table 1 – *Continued*

TOI	Separation (″)	P.A. (deg)	Contrast (I-band)	T_{eff} (K)	Distance (pc)	Proj. Sep.[a] (AU)	Radius correction factor (primary host)	Radius correction factor (secondary host)	Prev. det.?	WDS DD
433	4.0098	324.5	2.9	8543	498	1996	1.034	3.795	3	A3013
454	3.8682	256.7	2.2	6849	78	301	1.064	2.877	2	I56
455	1.0333	317.5	0.7	3562	20	20	1.235	1.608	2	RST2292BC
462	0.167	196.1	0.3	5205	205	34	1.326	1.497	1	
463	0.8084	215.0	3.5	6497	177	143	1.02	4.761	1	
476	0.6568	145.4	4.6	7691	226	148	1.007	8.153	1	
487	0.5111	201.0	1.2	5450	125	63	1.154	1.932	2	B2084AB
487	2.993	130.2	5.1	5450	125	374	1.005	10.138	1	
494	2.2257	153.7	5.7	4985	100	222	1.003	13.599	1	
498	2.1845	251.5	3.5	6218	176	384	1.02	4.914	3	RST4412AB
522	0.753	241.1	4.9	7381	109	82	1.005	9.342	1	
527	0.2211	255.9	2.1	7403	163	36	1.07	2.738	1	
550	0.6009	116.1	1.7	5076	62	37	1.1	2.269	1	
563	0.3841	33.4	0.8	5383	157	60	1.216	1.694	1	
568	0.2946	190.7	0.8		305	89	1.216		2	HDS1310
570	2.1638	110.6	6.6	5973	176	380	1.001	19.856	1	
575	0.6293	13.9	4.7	6529	173	108	1.007	8.367	1	
579	0.3303	202.6	3.3	4867	456	150	1.024		1	
593	0.5794	169.7	3.9	7034	411	238	1.014	5.597	1	
594	2.8688	45.3	0.4		308	883	1.301		3	B1595
598	1.7109	290.5	6.2	8324	581	994	1.002	16.803	1	
601	0.1512	352.5	3.1	6106	255	38	1.028	4.219	1	
602	0.976	164.4	3.7	7649	615	600	1.016	5.436	1	
605	0.6548	315.5	1.1	8265	508	332	1.168	1.938	2	JSP296
608	0.248	44.4	0.1	8323	500	124	1.383	1.397	2	RST2587
609	0.3001	91.1	4.0	6272	154	46	1.012	6.107	1	
611	2.3787	93.3	5.5	5689	96	228	1.003	12.33	3	
612	2.0252	98.7	3.9	6422	284	575	1.014	5.69	1	
612	0.1728	145.2	1.5	6422	284	49	1.119	2.079	1	
619	0.2797	234.6	1.0	5096	806	225	1.182		1	
621	2.0655	19.2	6.5	7850	186	384	1.001	19.256	1	
630	0.2099	315.8	3.6	6849	295	61	1.018	5.245	1	
635	1.7656	260.4	4.8	5914	58	102	1.006	9.176	1	
637	2.3926	332.9	5.1	5637	63	150	1.005	10.059	3	
640	0.2498	85.2	4.8	6587	341	85	1.006	8.756	1	
642	0.9513	238.0	2.6		422	401	1.045		1	
644	1.758	132.4	0.4	6112	1330	2338	1.301		2	RST2447
645	4.0745	109.0	1.9	5415	391	1593	1.083	2.505	3	
649	2.6777	130.3	3.2		430	1151	1.026		1	
651	3.608	191.7	2.2		86	310	1.064		3	BU17AB
658	3.88	67.2	0.7	6521	245	950	1.235	1.627	3	HJ4275
659	3.8774	67.2	1.0	5990	201	779	1.182	1.779	3	
666	0.248	257.4	2.8	6680	149	36	1.037	3.601	1	
676	1.5023	260.6	1.5	5430	545	818	1.119	2.151	3	
680	0.7809	331.0	4.3	5967	158	123	1.009	6.942	1	
684	0.2974	303.3	3.1	9488	580	172	1.028	4.103	1	
690	0.2221	292.4	1.2	5538	144	31	1.154	2.026	1	

Table 1 – *Continued*

TOI	Separation (″)	P.A. (deg)	Contrast (I-band)	T_{eff} (K)	Distance (pc)	Proj. Sep.[a] (AU)	Radius correction factor (primary host)	Radius correction factor (secondary host)	Prev. det.?	WDS DD
697	1.1597	138.2	4.9	5447	92	106	1.005	9.255	1	
697	0.0709	165.9	0.2	5447	92	6	1.353	1.43	1	
703	1.4153	221.8	4.7	5384	111	157	1.007	8.449	1	
758	0.1738	349.0	1.1	6072	154	26	1.168	1.907	1	
759	2.694	234.6	3.6	6107	660	1778	1.018	5.257	3	
772	2.3419	165.3	5.8	5184	130	304	1.002	14.246	3	
779	1.5378	165.3	4.8		273	419	1.006		1	
831	0.167	327.9	1.4	5808	86	14	1.129	1.941	2	RST1830
832	3.2133	63.9	4.7	5623	278	893	1.007	8.384	1	
837	2.3128	281.7	4.6	6513	136	314	1.007	7.995	3	
847	1.2446	317.1	0.7	6055	659	820	1.235		3	
851	1.8583	253.8	5.2	5782	155	288	1.004		3	
905	2.2757	100.8	5.9	5565	153	348	1.002	15.332	3	
906	1.246	50.8	2.8	5954	138	171	1.037	3.575	2	RST805
907	3.6665	52.0	1.1	6272	307	1125	1.168	1.852	3	
914	0.104	171.3	0.1	5321	233	24	1.383	1.35	1	
926	0.1903	159.6	2.2	5621	216	41	1.064	2.802	1	
930	0.692	32.6	2.5	6380	99	68	1.049		2	B1455
931	0.1118	56.8	0.3	6434	691	77	1.326		1	
952	1.1682	135.0	4.7	7025	461	538	1.007	8.607	1	
952	0.1176	59.4	3.6	7025	461	54	1.018	5.245	1	
954	2.3471	50.2	6.2	5820	232	544	1.002	15.699	1	
1033	0.2684	220.4	1.7	6113	219	58	1.1	2.367	1	
1049	1.2782	154.2	5.6	6599	389	497	1.003	12.617	1	

Table 1 Notes. – Columns (1-4) gives the properties of companions to TOIs detected by SOAR. Column (5-6) gives the effective temperature and distance to the TOI given in the TIC (Stassun et al. 2019). Column (7) gives the projected separation of the companion (assuming it is physically associated with the primary), derived from the on-sky separation measured by SOAR and the distance to the star. Columns (8-9) give the radius correction factor for hosted planets in each system due to the contamination from the detected star in the scenario where the primary is the planetary host and the scenario in which the physically associated secondary is the planetary host. Column (10) is a flag denoting a previous detection of each companion. The flags are **(1)**: new pair, contamination not included in the TIC; **(2)**: known pair, contamination not included in the TIC; **(3)**: known pair, contamination included in the TIC. Column (11) provides the discoverer designation code if the companion is in the Washington Double Star Catalog maintained by the USNO. Explanations for codes are available at https://www.usno.navy.mil/USNO/astrometry/optical-IR-prod/wds/WDS.

3.1. *Implications for TESS planet radii*

As discussed in Section 2.3, the additional flux from a stellar companion will dilute the transit signal in the TESS light curves, resulting in an underestimated planetary radius. We report the radius correction factors for planet candidates hosted in resolved binaries in our survey in Table 1.

In general, the identity of the host star for an S-type planet in a close binary is ambiguous (Horch et al. 2014), although there is evidence that typically the primary is more likely to be the planet host (Gaidos et al. 2016). We, therefore, report correction factors for each host scenario. Overall, we find a mean correction factor of 1.11 in the cases where all the planets orbit the primary stars. This is similar to the factor of 1.08 found for *Kepler* planets (Ziegler et al. 2018b) under the same assumption. Likewise, if all planets orbit the secondary stars which are bound to the primary[7], the radii of the planets will increase by a factor of 2.55 on average. This is slightly less than 3.29 found for *Kepler* planets (Ziegler et al. 2018b), which is likely due to the lower number of field stars detected in the TESS sample (see Section 2.4). Indeed, if a faint field companion is considered as

[7]Not every TESS planet candidate host had stellar radius estimates in the TIC or Gaia DR2. These targets are only included in calculating the mean correction factors in the case in which the primary star is assumed to be the host. In this case, only the flux contribution of the primary star is needed to determine the correction factor, as seen in Equation 1.

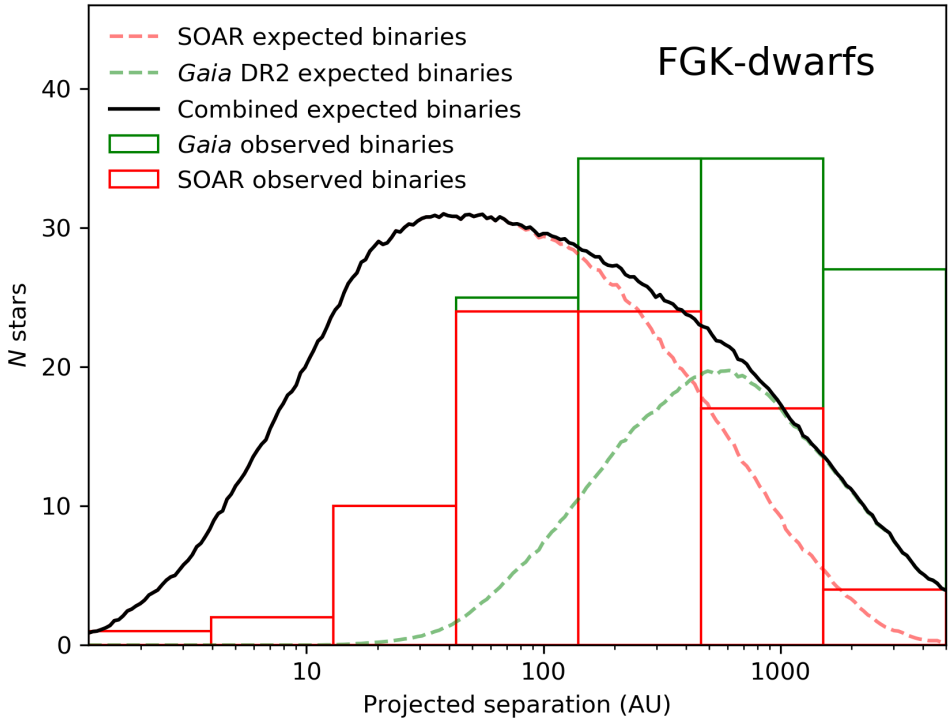

Figure 5. In red and green, the number of observed companions from SOAR and in Gaia DR2 for solar-type TESS planet candidate hosts in logarithmic bins of projected separation of 0.5 dex width. Companions found in both SOAR and Gaia are included in the SOAR sample. In black is the expected distribution from a multiplicity study of field stars (Raghavan et al. 2010), combining both field binaries that would be detected by SOAR and Gaia. The expected binaries from SOAR and Gaia, individually, are also plotted. These distributions take into account the detection sensitivity of both SOAR and Gaia. The observed distribution shows a clear paucity of TESS planet candidate host binaries at small projected separations compared to the field stars, and the inverse at wide separations.

bound, its estimated radius is small, and the resulting correction factor for the radius of a planet orbiting this companion becomes large.

In perhaps a more realistic scenario where planets are equally likely to orbit the primary or secondary star, we find an average correction factor of 1.82. This again is slightly lower than the correction factor of 2.18 found with similar assumptions in the *Kepler* survey.

We can restrict our separation range to reduce the fraction of unassociated stars in our sample. Within 1″, we find mean correction factors of 1.14, 1.90, and 1.55 under the assumptions that all primary stars host the planets, all secondary stars host the planets, and that either star is equally likely to host the planet, respectively. The latter figure, more probable than either of the other cases, is in agreement with the radius corrections of 1.6, 1.64, and 1.54 found for the *Kepler* planets by Ciardi et al. (2015), Hirsch et al. (2017), and Ziegler et al. (2018b), respectively.

3.2. *Close binary inference with Gaia DR2*

While Gaia DR2 typically can not resolve binaries with separations less than approximately 0.″7 (Ziegler et al. 2018a), the additional source does often result in spurious astrometric solutions. The reliability of the Gaia astrometry is quantified by the re-normalised unit weight error (RUWE)[8], which is near 1.0 for single sources, with a greater value (for instance, >1.4) indicating a non-single or otherwise extended source. Sources with only a two-parameter astrometric solution have null RUWE values.

We find that, for the 135 observed TESS planet candidate hosts observed with SOAR with RUWE values >1.4, 114 had resolved companions. Twelve of the observed targets had null RUWE values and all 12 had bright, close companions (Δmag< 2 and 0.″1< ρ < 0.″5). Combing both the high and null RUWE observed targets, approximately 86% had companions, typically within the Gaia DR2 binary resolution limit of 0.″7. The

[8]Described in detail in the Gaia DPAC public document, *Source Identifiers Assignment and Usage throughout DPAC*, document code GAIAC3TNARIBAS020 available from https://www.cosmos.esa.int/web/gaia/public-dpac-documents

RUWE values and properties of resolved systems are plotted in Figure 4.

It is unclear why some single stars (21 out of 391 observed) have high RUWE values. One possibility is the number of Gaia observations of each star. Gaia uses a scanning law that passes through the north and south ecliptic poles every six hours, resulting in approximately twice as many observations at mid-ecliptic latitudes as near the ecliptic plane or poles (Gaia Collaboration et al. 2016). A Kolmogrov-Smirnov test, however, finds the distribution of ecliptic latitudes for single stars with high and low RUWE values to be similar. The distribution of Gaia magnitudes and nearby stellar densities (determined in Section 2.4, of single stars with high and low RUWE values were also similar.

Checking for a high or null RUWE value can serve as an excellent first check for potential companion stars in TESS systems, although further high-resolution observations would still be required to determine the properties of a purported companion. The clustering of binary systems with null RUWE values in a region of similar separation and magnitude difference may, however, could even be used to infer the vague properties of a subset of the unresolved stars in Gaia DR2.

4. IMPACT OF BINARY STARS ON THE TESS PLANETARY SYSTEMS

The presence of a binary companion can result in a dynamically harsh environment, reducing the probability that a planetary system can form and survive. Some planets are found in close binary systems, however. In this section, we search for further insight into the impact binary stars have on the TESS planet population.

4.1. *Preparation of the sample*

To facilitate an analysis into the multiplicity of our observed targets, some sample preparation was required. As discussed in Section 2.4, we expect that few unassociated stars will be detected near our targets. However, as found in previous studies (Kraus et al. 2016; Ziegler et al. 2018c), most field companions will have a high contrast and large separations. We, therefore, remove from our sample companions with contrasts greater than 4 magnitudes and separations greater than $2''$.

The speckle imaging is a snapshot of the host systems, providing an angular separation between the primary and secondary star. To determine the projected physical separations, the distance to each system is required. We collect distances to each of these targets from Gaia DR2 (Bailer-Jones et al. 2018), when available. However, Gaia can provide spurious astrometric solutions in the case of close, unresolved binaries (Arenou et al. 2018). So, when Gaia distance errors are large (greater than 20%), we use the distances reported in the TIC (Stassun et al. 2019), which were derived using inverse Stefan-Boltzmann relations based on V magnitudes. The distances used for each target in this analysis are available in Table 5 in the Appendix.

We prepare our sample by removing stars with T_{eff} in the TIC inconsistent with an FGK-type star (i.e., $T_{eff} > 7200$ K and < 3900 K), using the relations of Pecaut et al. (2012). We also remove binaries with contrasts indicating mass ratios $q < 0.4$, as these are significantly more likely to be chance alignments (Kraus et al. 2016; Ziegler et al. 2018c). We determine q by finding the mass of the primary star based on its likely spectral type, estimated using the T_{eff} reported in the TIC, and the secondary star based on the magnitudes difference with the primary (Kraus & Hillenbrand 2007). We also remove systems with a TESS follow-up disposition of false positive, and systems with only a single transit detected by TESS. After these cuts, our sample includes 455 stars observed with SOAR.

To improve our coverage of wide binaries, we include companions to these 455 SOAR targets found in Gaia DR2 (Gaia Collaboration et al. 2018) with proper motions and distance estimates (Bailer-Jones et al. 2018) consistent at 2σ. We search out to an on-sky angular radius equivalent to a 5000 AU projected separation based on the Gaia distance estimate. El-Badry & Rix (2018) found that the proper motion of wide binaries can vary significantly because of orbital motion. For each star, we calculate the maximum Keplerian orbital on-sky motion as a function of projected separation. The proper motion of each nearby Gaia star is allowed to vary by this orbital motion in our binary detection. The Gaia DR2 binaries used are listed in Table 4 in the Appendix. Only pairs of stars with contrasts consistent with mass ratios $q > 0.4$ were included. Ziegler et al. (2018a) provided the binary recovery sensitivity of Gaia DR2.

4.2. *Multiplicity of solar-type TESS planet candidate hosts*

Close binaries can provide many potential obstacles to planet formation and evolution. In a large survey of *Kepler* planets, Kraus et al. (2016) found that far fewer planets were detected around stars with companions at solar system scales, within approximately 50 AU. The TESS sample is quite disparate in several ways from the *Kepler* sample, as shown in Figure 1. In general, the TESS planets are somewhat larger and at shorter periods than the *Kepler* planets, a consequence of the TESS photometric precision and survey strategy. Unlike *Kepler*, the TESS planets are spread across the sky and sample a more diverse set of the Galactic stellar popu-

lation, providing an opportunity to confirm and characterize the effect of binaries

To understand how binaries impact planetary systems, we compare our sample to a simulated survey of field solar-type stars. We use the field binary statistics of Raghavan et al. (2010), who found a flat eccentricity, a log-normal period distribution, and a nearly uniform mass ratio distribution in the population of solar-type field binaries. We follow the procedures of Kraus et al. (2016) to account for projection effects, Malmquist bias, and the detection limits of our survey. We also account for the reduced sensitivity of TESS to planet transits due to dilution by the stellar companion.

For each solar-type star observed in our survey, a Monte Carlo model was constructed to determine the expected number of binary companions at a range of projected separations between 1-5000 AU. In each of 10^5 iterations, a companion star was populated at a probability equal to the product of the multiplicity of solar-type stars, 44%, and, since binaries are over-represented in flux-limited surveys (Schmidt 1968), we correct for Malmquist bias by adding a weighting equal to the fractional volume excess in binaries due to their relative brightness, V_{bin}/V_{single}. The period, eccentricity, and mass ratio of these binaries were drawn from the distributions reported in Raghavan et al. (2010). The period was converted to a semi-major axis using the TIC estimated stellar masses. We select uniformly distributed values for the cosine of inclination, the position angle of ascending node, the longitude of periastron, and the time of periastron passage. Finally, the instantaneous separation was projected to the distance to the primary star as reported in Gaia DR2. The mass ratio was converted to an approximate magnitude contrast using the relations in Kraus & Hillenbrand (2007), and possible detection by SOAR speckle imaging and Gaia DR2 was determined using the measured sensitivity limits and the companion's contrast and separation. We use the ratio of non-detected binaries to the total number of binaries at each separation to determine a completeness correction due to limitations in the ability to resolve close or wide companions.

The resulting observed binaries of TESS planet candidate hosts from SOAR and Gaia compared to the expected number derived for field stars is shown in Figure 5. The observed companion rate to the TESS planet candidates as a function of projected separation was determined by dividing the number of observed binaries by the total number of stars observed. The companion rate in each separation bin was then corrected for survey completeness using our measured sensitivity limits. The companion rates for the TESS planet candidate hosts and field solar-type stars are shown in Figure 6. The distributions differ substantially, both at close and wide separations, which we will address in turn.

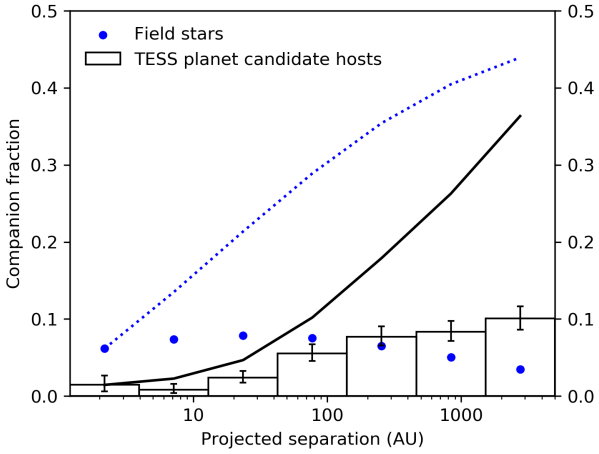

Figure 6. The observed companion rates for the solar-type TESS planet candidate hosts, corrected for survey completeness, for logarithmic bins with width of 0.5 dex is shown by the black bars. The completeness factors are based on the binary statistics of Raghavan et al. (2010) and our detection limits. The estimated companion rates for field stars, plotted by blue points, are included for comparison. The cumulative distributions for the TESS planet candidates and field stars are plotted as dotted and solid lines, respectively.

4.2.1. *Suppression of planet-hosting close binaries*

We find significantly fewer binaries in the TESS sample with projected separations of less than 100 AU than would be expected for a similar survey of field stars (44 observed binaries compared to an expectation of 125±8, a 9.1σ discrepancy). We find a completeness corrected companion rate for TESS planets hosts of $9.7^{+1.5}_{-1.3}$% at projected separations of less than 100 AU and larger than 1 AU. For comparison, we estimate for field stars a companion rate at similar projected separations of $27.7^{+2.0}_{-2.2}$%, using the binary statistics of Raghavan et al. (2010). TESS planet hosts are therefore approximately 3× less likely to have a close binary companion, compared to field stars.

Similar to Kraus et al. (2016), the dearth of close binaries for planet hosts can be modeled by a simple two parameter model, using a suppression factor, S_{bin}, that cuts on at some semi-major axis value, a_{cut}. We performed a Markov chain Monte Carlo (MCMC) analysis to explore 10^6 possible values for S_{bin} and a_{cut}, seeking to reduce the χ^2 goodness of fit to the observed distribution. The resulting distributions are shown in Figure 7. We find an optimal values for the suppression with 68% credibility ranges to be $S_{bin}=24^{+11}_{-7}$% and $a_{cut}=46^{+22}_{-15}$ AU, shown in Figure 8. These values are in agree-

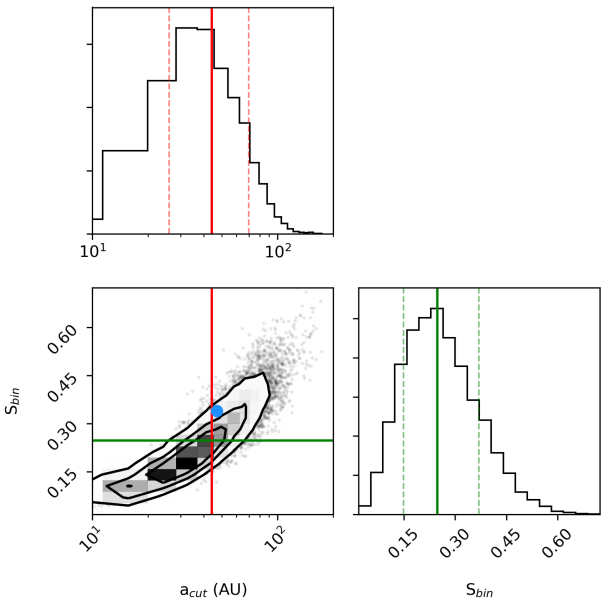

Figure 7. The distributions of suppression factors and semi-major axis cuts from 10^6 chains of an MCMC analysis to model the observed close binary suppression seen in systems with TESS planet candidates. Solid lines indicate the median value of each distribution (a_{cut}=46 AU and S_{bin}=0.24) and dashed lines mark the 68% confidence interval. The two parameters are correlated, such that less suppression is required if the semi-major axis cutoff is larger, and vice versa. A blue circle marks the values of the best fit model from the *Kepler* sample of Kraus et al. (2016).

ment with those found by Kraus et al. (2016) for *Kepler* planet candidates (S_{bin}=34^{+15}_{-14}% and a_{cut}=47^{+59}_{-23} AU), and again the null hypothesis (i.e., the field and planet candidate host distribution are similar with no binary suppression occurring) is strongly disfavored at 9.8σ.

4.2.2. *Enhancement of wide binaries in systems with large planets*

At wide separations, more binaries were detected around the TESS planet candidate hosts compared to the field stars: 119 observed binaries with projected separations greater than 100 AU, compared to an expected number of 77±7, a 4.9σ discrepancy.

The wide binaries being detected are almost exclusively those hosting the large planet candidates. This is readily apparent if we split our sample into two bins using a radius cut of 9 $R_\oplus$ (approximately the size of Saturn), as shown in Figure 9. We find that both populations of 244 small and 199 large planets exhibit a paucity of systems in close binaries. At wide separations, however, the companion rates for the two populations diverge: at projected separations greater than 200 and 10^3 AU, large planet hosts have a completeness corrected companion rate of 47.8±3.8% and 30.4±3.4%, respectively. For small planet hosts, the companion rates for similar projected separation ranges are $6.4^{+1.5}_{-1.1}$% and $1.8^{+1.3}_{-0.7}$%, respectively. Thus, the two populations have discrepant companion rates for projected separations greater than 200 and 10^3 AU with significances of 9.8σ and 8.1σ, respectively.

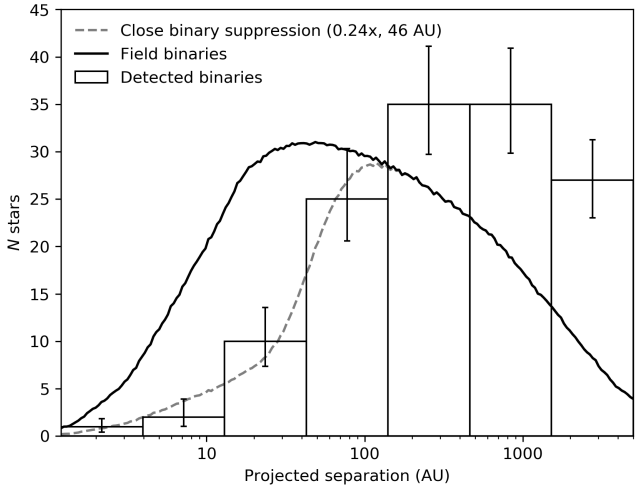

Figure 8. The number of observed solar-type TESS planet candidate hosts found with stellar companions and the best fit model for close binary suppression applied to the expected distribution of binaries for field stars. The best fit model has binaries suppressed by a factor of 0.24 at physical separations less than 46 AU.

The companion rates for the small and large planets at wide separations are also both significantly divergent from that of field stars. We estimate from the distribution of Raghavan et al. (2010) that field stars have a companion rate of 13.7% and 5.3% at projected separations greater than 200 and 10^3 AU, respectively. Therefore, large TESS planets are approximately a factor of 3.5 more likely to be hosted in a wide binary than would be expected. Conversely, small TESS planets are 2× *less* likely to be found in a wide binary system than would be expected from field star statistics.

4.3. *Binary fraction of M-dwarf planet candidate hosts*

We observed 44 planet candidate hosts with T_{eff} estimates in the TIC consistent with an M-dwarf (T_{eff} <3900 K, Pecaut et al. (2012)). We detected companions to 16 of these hosts, for a companion fraction of 36±9%. This is consistent with the field star M-dwarf multiplicity fraction of 26.8±1.4% found by Winters et al. (2019).

To compare the separation distribution of planet candidate M-dwarf hosts to the field star population we use the companion fraction, the log-normal projected sepa-

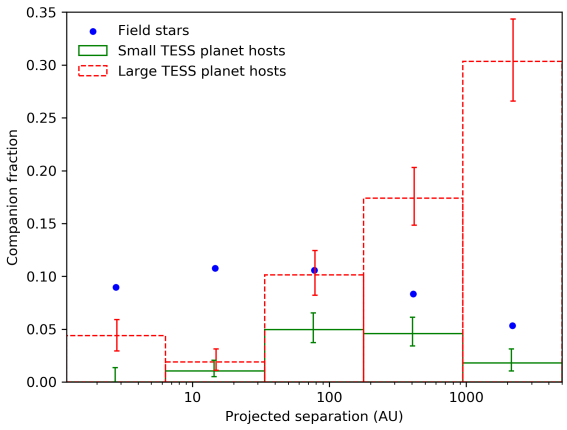

Figure 9. The completeness corrected companion fraction per 0.5 dex bins in projected separation for small and large TESS planet candidate hosts observed in this survey. For reference, the separation distribution of field binaries from Raghavan et al. (2010) is included. Both populations of TESS planet hosts have suppressed rates of close binaries, but have diverging binary rates at wide projected separations. Large planets (R_p >9 $R_\oplus$) are approximately 3.5× more likely to be found in a wide binary, compared to field stars. Conversely, small planets are 2× less likely to be found in a wide binary.

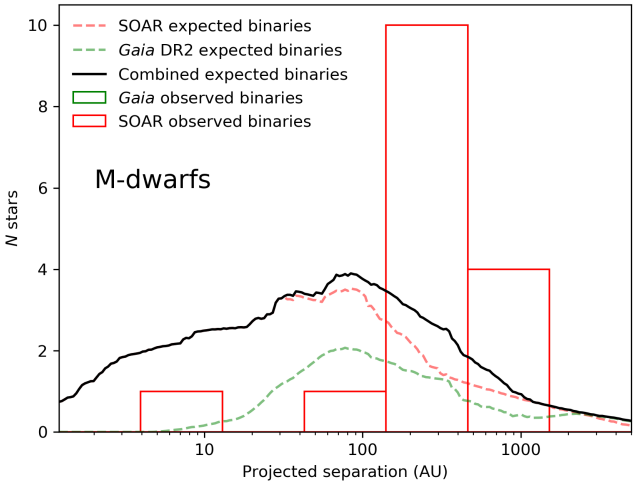

Figure 10. Similar to Figure 5 for TESS M-dwarf planet candidate hosts, using the field binary statistics of Winters et al. (2019). As with the solar-type stars, the M-dwarf planet candidate hosts have a deficit of close binaries at separations less than 100 AU, and a surplus of wide binaries separated by more than 100 AU.

ration distribution (peaking at 20 AU with σ_{loga}=1.16), and the uniform mass ratio distribution (with a slight increase in near-equal mass binaries) found by Winters et al. (2019). The resulting distribution is shown in Figure 10.

We find fewer close binaries than would be expected to the M-dwarf planet candidate hosts: 2 observed compared to approximately 11 expected at projected separations of less than 100 AU. We also find a large number of companions at wider separations: 14 observed companions at projected separations between 100 and 5000 AU, compared to approximately 5 that would be expected.

Both of these results mirror those found with the solar-type sample. We do not see a large number of companions at very wide projected separations (s>1000 AU). This may, in part, be due to the M-dwarf projected separation distribution peaking at lower separations (∼20 AU rather than ∼50 AU) and with lower variance than the solar-type sample. Also, as shown in Section 4.2.2, the widest binaries typically host Jupiter-size planets, which are inherently rare around M-dwarfs (Dressing & Charbonneau 2013).

4.4. *Mass ratios of planet candidate host binaries*

The mass ratio, or q, distribution of solar-type binary systems was found to be nearly uniform by Raghavan et al. (2010), with an increase for near-equal mass binaries. Winters et al. (2019) found a similar distribution at high-q for M-dwarfs. Ngo et al. (2016) found that mass ratio distribution for hosts of hot Jupiters was heavily weighted towards low-q companions.

To compare the distribution in the SOAR detections, we use the mass estimates based on the TIC T_{eff} estimates for the primary, and a mass consistent with a suitably fainter star for the secondary (Kraus & Hillenbrand 2007). For the expected number of field stars, we use the results of the simulation described in Section 4.2, which takes into account our survey sensitivity.

The observed and expected mass ratio distribution of binaries to TESS planet candidate hosts is shown in Figure 11. The mass ratio distribution of observed binaries is consistent with being uniform for $q > 0.3$; for lower mass ratios the SOAR sensitivity is low. There is no significant difference in the distribution for small and large planets (cut at 9 $R_\oplus$). Compared to the expected number based on field star statistics, we find slightly fewer high-q binaries, due in part to binary suppression at low separations, and slightly more low-q binaries, which is likely to be, at least in part, a consequence of unassociated field star contamination as the companions with large magnitude differences are at wide separations.

5. BINARY IMPACT ON THE GALACTIC PLANET POPULATION

Approximately half of solar-type field stars in our galaxy are found with a stellar companion, and, as discussed in Section 1, the impact binaries have on the planet population is potentially large. The TESS sam-

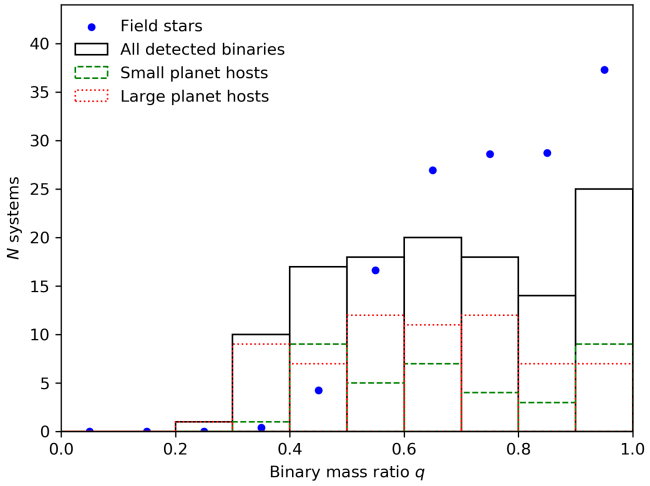

Figure 11. The mass ratio distribution of all observed binaries to TESS planet candidates resolved in SOAR speckle imaging, including the individual distributions for large and small planet candidate hosting stars. The expected distribution of observed binaries based on the near-uniform mass ratio distribution of field stars (Raghavan et al. 2010) and the survey sensitivity is included. The observed mass distribution is consistent with uniform.

ple is not statistically complete, containing a combination of small planets, similar to the majority of planets detected by *Kepler*, and many large planets, similar to the extensively studied population of hot Jupiters (e.g., Wu et al. 2007; Knutson et al. 2014; Ngo et al. 2016; Evans et al. 2016). In our data, we see a combination of two separate effects found individually in previous studies: suppression of planets in binaries at low separations, and enhancement of binaries at wide separations.

Follow-up observations of the planet candidate hosts found in the *Kepler* survey gave some insight into how binaries impact planetary systems. Wang et al. (2015) found some evidence in RV trends that binaries at separations <100 AU may suppress planet occurrence. Kraus et al. (2016) found that approximately a fifth of solar-type stars are not able to host planets due to the influence of stellar companions. We find similar suppression of close binaries among the TESS planet candidates, suggesting this effect is likely prevalent throughout the Galaxy, in regions of varying stellar density and age. The suppression of close binaries is apparent regardless of cuts in the orbital period, planetary radii, or stellar effective temperature.

As noted by Kraus et al. (2016), it is not clear why some close binaries are able to host planets with all of the theoretical obstacles to their formation and survival. Many of the TESS binaries that are close in projection likely have short orbital periods, meaning their motion may be detected over the coming years. Continued monitoring can provide orbital solutions for these systems to find a true physical separation rather than the projected separation presented here. Studying these orbits may provide insight into the conditions that exist such that planets may form and survive in the chaotic regime around close binaries.

It is possible that the enhanced companion fraction for small planets may be, at least in part, due to observation effects: the false positive rate of giant planets in transiting planet surveys has been found to be larger than for smaller planets (Fressin et al. 2013). The radii of Jupiter-mass planets and brown dwarfs are similar, and mass constraints are required to confirm each planet. However, brown dwarfs on close transits seem to be inherently rarer than massive planets (Bowler 2016). In addition, while a planet is more likely to be hosted by the primary star in the majority of systems (Gaidos et al. 2016), multiple star systems will have some enhancement in planet occurrence due to having additional potential hosts.

The exclusion of previously confirmed planets from our target list, as discussed in Section 2, may result in a bias in our sample. Many of these confirmed planets were detected in ground-based surveys, which may avoid resolved binaries (Street et al. 2003; Bakos 2018) or avoid following-up systems with binary indicators, such as multiple sets of spectral lines (Triaud et al. 2017). In addition, the contamination from unresolved, near-equal-mass binaries may result in the non-detection of planets by ground-based surveys (Bouma et al. 2018). Some of these planets may subsequently be detected by TESS. These observational biases could result in an inflated companion rate for the newly detected TESS systems in our survey.

Previous binary surveys of large planet hosts that were detected exclusively from ground-based surveys find a similar enhancement in binaries at wide separations. Ngo et al. (2016) found that stars hosting hot Jupiters were approximately three times more likely to have stellar companions than field stars. Fontanive et al. (2019) found a wide binary fraction (20-10,000 AU separations) for gas giants approximately twice that of field stars. Similarly, Ziegler et al. (2018c) found that the large, close-in *Kepler* planets were significantly more likely to have companions than other populations of planets. We find a similar effect for our sample as a whole. However, closer analysis reveals this enhancement is due only to the systems hosting the largest planets. Indeed, a suppression effect is also seen for small planets in binaries at very wide projected separations (s >1000 AU).

There are two possible physical scenarios that could lead to a high companion fraction for systems hosting

hot Jupiters: first, the binary companion may encourage in some manner the formation of large planets; and second, large planets form at similar rates in single and multiple star systems, but in binaries, the companion star drives large planets inward to the low-period regime probed by TESS. For the former, there is evidence that a stellar companion can lead to density waves in the protoplanetary disks (Dong et al. 2015). These high-density regions can subsequently seed the formation of planetesimals (Carrera et al. 2015). In addition, the protoplanetary disks around binary stars may have more mass than around single stars, which simulations suggest leads to larger planets (Mordasini et al. 2012).

The high number of gas giants in binaries coupled with the low number of observed smaller planets may be explained by planet-planet scattering during migration. In other words, the orbits of inner smaller planets may be altered by the gas giants being driven inward to low-period orbits. In one possible scenario, Kozai-Lidov instabilities induced by the stellar companion may initially drive the gas giant to a highly eccentric orbit (Holman et al. 1997; Naoz et al. 2011). Ngo et al. (2016) and Fontanive et al. (2019) found that the Kozai-Lidov effect alone was insufficient to explain the observed population of hot Jupiters. In scattering events, large planets on wide orbits are preferred, as quantified by the Safronov number (Ford & Rasio 2008). The highly eccentric gas giant in this scenario would dominate the inner planets as it nears perihelion, resulting in planet scattering events (Fabrycky & Tremaine 2007). Eventually, the gas giant orbit will circularize to a low-period orbit due to planet-star tidal friction (Jackson 2009). Observational evidence suggests planetary interactions during secular migration are not unusual: around a quarter of hot Jupiters are found on retrograde orbits, only possible through close planetary perturbations (Naoz et al. 2011; Ngo et al. 2015).

Dynamical interactions between planets with high mass disparities may dramatically alter the orbital inclination of the smaller planet, in many cases to a non-transiting orientation (Hamers 2017), or drive the smaller planets to highly eccentric orbits (Xie et al. 2016), and possibly even ejection from the system (Davies et al. 2014). Planet-planet scattering has been shown to largely reproduce the observed distribution of eccentricities in transiting planets (e.g., Ford & Rasio 2008; Jurić & Tremaine 2008; Raymond et al. 2011). Numerical investigations suggest instabilities in giant planet orbits are likely destructive to inner terrestrial planets (Veras & Armitage 2006; Matsumura et al. 2013). Indeed, *Kepler* found only a small fraction of small, close-in planets had gas giants in nearby orbits (Lissauer et al. 2011; Ciardi et al. 2013; Huang et al. 2016). Lastly, Wang et al. (2015) found that systems hosting small planets had fewer companions than field stars at separations up to 1500 AU, compared to 100 AU for systems with hot Jupiters. As they note, another possible explanation for this disparity is that the relative timescales of pericenter and nodal precession increases as planetary mass decreases (Takeda et al. 2008). Thus for small planets, the Kozai timescale will be shorter than precession. Consequently, the weaker planet-planet coupling means smaller planets are more prone to the influence of distant stellar companions.

6. CONCLUSIONS

We searched 542 TESS planet candidate hosts for companions using SOAR speckle imaging. We found 123 companions within 3″ of 117 targets. Contamination from these companions in the TESS light curves results in the radii of planet candidates in these systems to increase by a factor of 1.11, assuming the primary star is indeed the host. We find that TESS planet candidate hosts are around 3.5× less likely to have stellar companions at projected separations less than approximately 50 AU than field stars. The destructive impact of close binaries, previously seen in the *Kepler* sample, is apparent in the local Galaxy. We also detect far more large planets, and far fewer small planets, in wide binaries then would be expected for field stars. This may be evidence of chaotic secular migration of gas giants, resulting from perturbations from the binary companion, inducing planet-planet scattering. The planet candidate hosting M-dwarfs have a similar binary pattern as the solar-type sample. The mass ratio distribution of planet candidate hosting stars is consistent with uniform, as is seen in field stars.

Future multi-band speckle observations by SOAR of the resolved binary systems hosting TESS planets will be able to determine the probability that the companions are indeed physically associated. In addition, multi-epoch observations over the coming years will be able to check for common proper motion and solve the orbits of bound systems, providing the semi-major axis and eccentricity of the binary systems hosting planets. Analysis of these binaries may provide insight into how some close systems were able to form and maintain their planetary populations. Lastly, the detection of Northern planet candidates by TESS, beginning in 2019, will provide many more nearby planet-hosting systems. Their proximity will allow efficient instruments on moderate size telescopes in the North, such as Robo-AO on the University of Hawaii 88-in (Baranec et al. 2017), to detect companions at Solar system scales.

ACKNOWLEDGMENTS

C.Z. is supported by a Dunlap Fellowship at the Dunlap Institute for Astronomy & Astrophysics, funded through an endowment established by the Dunlap family and the University of Toronto. A.W.M was supported by NASA grant 80NSSC19K0097 to the University of North Carolina at Chapel Hill.

Based on observations obtained at the Southern Astrophysical Research (SOAR) telescope, which is a joint project of the Ministério da Ciência, Tecnologia, Inovações e Comunicações (MCTIC) do Brasil, the U.S. National Optical Astronomy Observatory (NOAO), the University of North Carolina at Chapel Hill (UNC), and Michigan State University (MSU).

This paper includes data collected by the TESS mission. Funding for the TESS mission is provided by the NASA Explorer Program. This work has made use of data from the European Space Agency (ESA) mission *Gaia* (https://www.cosmos.esa.int/gaia), processed by the *Gaia* Data Processing and Analysis Consortium (DPAC, https://www.cosmos.esa.int/web/gaia/dpac/consortium). Funding for the DPAC has been provided by national institutions, in particular the institutions participating in the *Gaia* Multilateral Agreement. This research has made use of the Exoplanet Follow-up Observation Program website, which is operated by the California Institute of Technology, under contract with the National Aeronautics and Space Administration under the Exoplanet Exploration Program. This work made use of the Washington Double Star Catalog maintained at USNO.

Facilities: SOAR (HRCam), TESS, Gaia

Software: astropy, emcee, corner

REFERENCES

Alexander, R. 2012, ApJL, 757, L29

Arenou, F., Luri, X., Babusiaux, C., et al. 2018, A&A, 616, A17

Bailer-Jones, C. A. L., Rybizki, J., Fouesneau, M., Mantelet, G., & Andrae, R. 2018, AJ, 156, 58

Bakos, G. Á. 2018, The HATNet and HATSouth Exoplanet Surveys, 111

Baranec, C., Riddle, R., & Law, N. M. 2017, arXiv e-prints, arXiv:1709.07103

Baranec, C., Ziegler, C., Law, N. M., et al. 2016, AJ, 152, 18

Baranec, C., Riddle, R., Law, N. M., et al. 2014, ApJ, 790, L8

Borucki, W. J., Koch, D., Basri, G., et al. 2010, Science, 327, 977

Bouma, L. G., Masuda, K., & Winn, J. N. 2018, AJ, 155, 244

Bowler, B. P. 2016, Publications of the Astronomical Society of the Pacific, 128, 102001

Carrera, D., Johansen, A., & Davies, M. B. 2015, A&A, 579, A43

Ciardi, D. R., Beichman, C. A., Horch, E. P., & Howell, S. B. 2015, ApJ, 805, 16

Ciardi, D. R., Fabrycky, D. C., Ford, E. B., et al. 2013, ApJ, 763, 41

Davies, M. B., Adams, F. C., Armitage, P., et al. 2014, in Protostars and Planets VI, ed. H. Beuther, R. S. Klessen, C. P. Dullemond, & T. Henning, 787

Deacon, N. R., Kraus, A. L., Mann, A. W., et al. 2016, MNRAS, 455, 4212

Dong, R., Hall, C., Rice, K., & Chiang, E. 2015, ApJL, 812, L32

Dotter, A., Chaboyer, B., Jevremović, D., et al. 2008, ApJS, 178, 89

Dragomir, D., Teske, J., Günther, M. N., et al. 2019, ApJ, 875, L7

Dressing, C. D., & Charbonneau, D. 2013, ApJ, 767, 95

El-Badry, K., & Rix, H.-W. 2018, MNRAS, 480, 4884

Espinoza, N., Brahm, R., Henning, T., et al. 2019, arXiv e-prints, arXiv:1903.07694

Evans, D. F., Southworth, J., Maxted, P. F. L., et al. 2016, A&A, 589, A58

Evans, D. F., Southworth, J., Smalley, B., et al. 2018, A&A, 610, A20

Fabrycky, D., & Tremaine, S. 2007, ApJ, 669, 1298

Fontanive, C., Rice, K., Bonavita, M., et al. 2019, MNRAS, 485, 4967

Ford, E. B., & Rasio, F. A. 2008, ApJ, 686, 621

Fressin, F., Torres, G., Charbonneau, D., et al. 2013, ApJ, 766, 81

Gaia Collaboration, Prusti, T., de Bruijne, J. H. J., et al. 2016, Astronomy and Astrophysics, 595, A1

Gaia Collaboration, Brown, A. G. A., Vallenari, A., et al. 2018, A&A, 616, A1

Gaidos, E., Mann, A. W., Kraus, A. L., & Ireland, M. 2016, MNRAS, 457, 2877

Hamers, A. S. 2017, ApJL, 835, L24

Henden, A. A., Welch, D. L., Terrell, D., & Levine, S. E. 2009, in American Astronomical Society Meeting Abstracts, Vol. 214, American Astronomical Society Meeting Abstracts #214, 669

Hirsch, L. A., Ciardi, D. R., Howard, A. W., et al. 2017, AJ, 153, 117
Holman, M., Touma, J., & Tremaine, S. 1997, Nature, 386, 254
Horch, E. P., Howell, S. B., Everett, M. E., & Ciardi, D. R. 2014, ApJ, 795, 60
Howard, A. W., Marcy, G. W., Bryson, S. T., et al. 2012, ApJS, 201, 15
Huang, C., Wu, Y., & Triaud, A. H. M. J. 2016, ApJ, 825, 98
Huang, C. X., Burt, J., Vanderburg, A., et al. 2018, ApJL, 868, L39
Jackson, B. K. 2009, PhD thesis, The University of Arizona
Jang-Condell, H., Mugrauer, M., & Schmidt, T. 2008, ApJL, 683, L191
Jones, M. I., Brahm, R., Espinoza, N., et al. 2019, A&A, 625, A16
Jurić, M., & Tremaine, S. 2008, ApJ, 686, 603
Knutson, H. A., Fulton, B. J., Montet, B. T., et al. 2014, ApJ, 785, 126
Kraus, A. L., & Hillenbrand, L. A. 2007, AJ, 134, 2340
Kraus, A. L., Ireland, M. J., Hillenbrand, L. A., & Martinache, F. 2012, ApJ, 745, 19
Kraus, A. L., Ireland, M. J., Huber, D., Mann, A. W., & Dupuy, T. J. 2016, AJ, 152, 8
Law, N. M., Morton, T., Baranec, C., et al. 2014, ApJ, 791, 35
Lissauer, J. J., Fabrycky, D. C., Ford, E. B., et al. 2011, Nature, 470, 53
Mann, A. W., Dupuy, T., Kraus, A. L., et al. 2019, ApJ, 871, 63
Matson, R. A., Howell, S. B., Horch, E. P., & Everett, M. E. 2018, AJ, 156, 31
Matsumura, S., Ida, S., & Nagasawa, M. 2013, ApJ, 767, 129
Mordasini, C., Alibert, Y., Benz, W., Klahr, H., & Henning, T. 2012, A&A, 541, A97
Morton, T. D., Bryson, S. T., Coughlin, J. L., et al. 2016, ApJ, 822, 86
Morton, T. D., & Johnson, J. A. 2011, ApJ, 738, 170
Naoz, S., Farr, W. M., Lithwick, Y., Rasio, F. A., & Teyssandier, J. 2011, Nature, 473, 187
Naoz, S., Farr, W. M., & Rasio, F. A. 2012, ApJL, 754, L36
Ngo, H., Knutson, H. A., Hinkley, S., et al. 2015, ApJ, 800, 138
—. 2016, ApJ, 827, 8
Pecaut, M. J., Mamajek, E. E., & Bubar, E. J. 2012, ApJ, 746, 154
Quinn, S. N., Becker, J. C., Rodriguez, J. E., et al. 2019, arXiv e-prints, arXiv:1901.09092
Quintana, E. V., Adams, F. C., Lissauer, J. J., & Chambers, J. E. 2007, ApJ, 660, 807
Raghavan, D., McAlister, H. A., Henry, T. J., et al. 2010, ApJS, 190, 1
Raymond, S. N., Armitage, P. J., Moro-Martín, A., et al. 2011, A&A, 530, A62
Ricker, G. R., Winn, J. N., Vanderspek, R., et al. 2014, in Society of Photo-Optical Instrumentation Engineers (SPIE) Conference Series, Vol. 9143, Space Telescopes and Instrumentation 2014: Optical, Infrared, and Millimeter Wave, 914320
Rodriguez, J. E., Quinn, S. N., Huang, C. X., et al. 2019, AJ, 157, 191
Schmidt, M. 1968, ApJ, 151, 393
Skrutskie, M. F., Cutri, R. M., Stiening, R., et al. 2006, AJ, 131, 1163
Stassun, K. G., Oelkers, R. J., Pepper, J., et al. 2018, AJ, 156, 102
Stassun, K. G., Oelkers, R. J., Paegert, M., et al. 2019, arXiv e-prints, arXiv:1905.10694
Street, R. A., Pollaco, D. L., Fitzsimmons, A., et al. 2003, in Astronomical Society of the Pacific Conference Series, Vol. 294, Scientific Frontiers in Research on Extrasolar Planets, ed. D. Deming & S. Seager, 405–408
Takeda, G., Kita, R., & Rasio, F. A. 2008, ApJ, 683, 1063
Tokovinin, A. 2018, PASP, 130, 035002
Triaud, A. H. M. J., Martin, D. V., Ségransan, D., et al. 2017, A&A, 608, A129
Vanderburg, A., Huang, C. X., Rodriguez, J. E., et al. 2019, arXiv e-prints, arXiv:1905.05193
Veras, D., & Armitage, P. J. 2006, ApJ, 645, 1509
Wang, J., Fischer, D. A., Xie, J.-W., & Ciardi, D. R. 2015, ApJ, 813, 130
Welsh, W. F., Orosz, J. A., Carter, J. A., et al. 2012, Nature, 481, 475
Winters, J. G., Henry, T. J., Jao, W.-C., et al. 2019, AJ, 157, 216
Wizinowich, P. L., Le Mignant, D., Bouchez, A. H., et al. 2006, PASP, 118, 297
Wu, Y., Murray, N. W., & Ramsahai, J. M. 2007, ApJ, 670, 820
Xie, J.-W., Dong, S., Zhu, Z., et al. 2016, Proceedings of the National Academy of Science, 113, 11431
Ziegler, C., Law, N. M., Morton, T., et al. 2017, AJ, 153, 66
Ziegler, C., Law, N. M., Baranec, C., et al. 2018a, AJ, 156, 259
—. 2018b, AJ, 155, 161
—. 2018c, AJ, 156, 83

APPENDIX

Table 2. TIC matches to resolved binaries detected by SOAR

TOI	TIC Primary	TIC Secondary	SOAR Sep. (″)	SOAR P.A. (°)	SOAR Contrast (mag)	TIC Sep. (″)	TIC P.A. (°)	TIC Contrast (mag)
123	290131778	1992266045	1.2894	294.6	1.8	1.37	292.2	1.66
128	391949880	675054894	2.2195	153.8	2.4	2.17	153.2	2.51
147	220435095	685140266	2.6583	217.6	4.6	2.65	217.8	4.81
149	260985861	675057530	1.117	132.6	0.1	0.73	132.0	0.82
167	149990841	737110430	0.1593	306.6	0.8	0.39	126.0	0.06
180	51912829	615712419	1.2682	63.7	4.3	1.69	60.8	4.15
240	101948569	616347276	2.3656	197.6	3.1	2.3	197.7	3.19
253	322063810	616169972	2.6623	351.2	4.0	2.58	353.9	3.82
258	350445771	734530071	2.0749	343.2	2.9	2.07	343.5	2.93
343	66497310	2052060639	2.8471	321.0	4.5	2.68	321.0	4.93
386	238059180	767048826	1.1739	274.4	3.5	1.21	276.1	3.21
387	92359850	651667037	2.2878	342.9	3.2	2.28	341.9	3.45
427	70914192	686486697	2.6122	152.9	4.8	2.62	152.6	4.95
433	188989177	188989178	4.0098	324.5	2.9	3.98	324.0	2.85
498	121338379	803532221	2.1845	251.5	3.5	2.62	259.0	3.42
594	146406806	824851862	2.8688	45.3	0.4	2.47	46.0	0.75
611	154459165	831946954	2.3787	93.3	5.5	1.93	105.0	5.83
637	133334108	821927265	2.3926	332.9	5.1	2.41	330.4	5.02
645	157568289	157568287	4.0745	109.0	1.9	4.07	108.9	1.88
651	293689267	293689266	3.2615	219.3	1.5	3.68	39.3	-0.47
658	48476907	48476908	3.88	67.2	0.7	3.87	68.4	0.71
659	48476908	48476907	3.8774	67.2	1.0	3.87	248.4	-0.71
676	219187649	901927162	1.5023	260.6	1.5	1.5	261.2	1.9
759	152147232	942050885	2.694	234.6	3.6	2.69	236.0	3.56
772	286864983	951863424	2.3419	165.3	5.8	2.45	176.9	5.84
837	460205581	847769574	2.3128	281.7	4.6	2.31	280.9	4.7
851	40083958	610472559	1.8583	253.8	5.2	1.92	253.1	5.59
847	231289421	650780404	1.2446	317.1	0.7	0.85	320.9	1.09
905	261867566	1105898342	2.2757	100.8	5.9	2.14	101.5	6.21
907	305424003	1510534043	3.6665	52.0	1.1	3.64	52.1	1.0

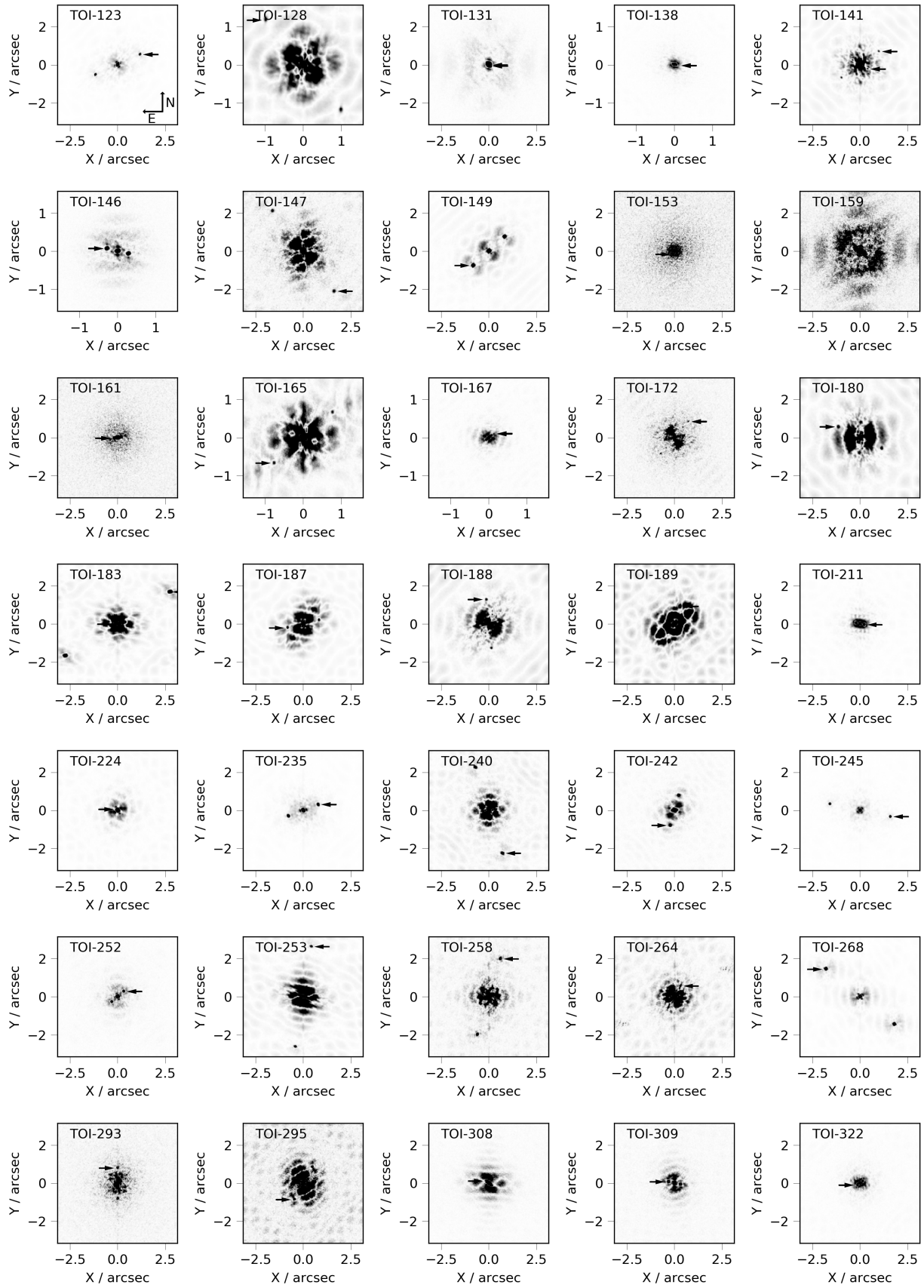

Figure 12. Speckle auto-correlation functions from SOAR speckle observing of TESS planet candidate hosts stars with resolved nearby stars. Each nearby star is mirrored in the images, with the true location marked by an arrow. Images are presented with an inverse linear scale for clarity. The orientation is similar in all images, with North pointed up and East to the left. A compass is shown in the top left image for reference.

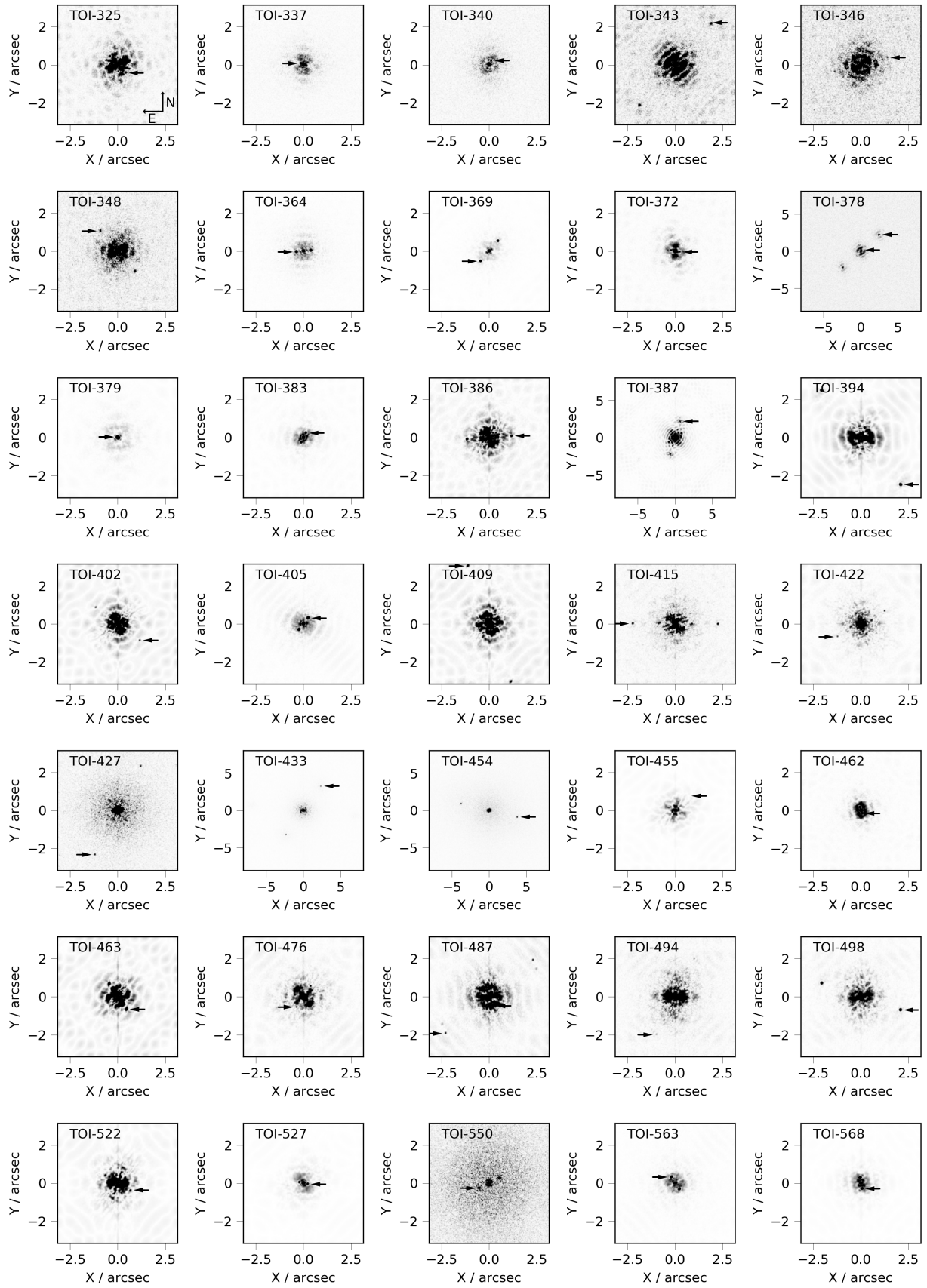

Figure 13. Similar to Figure 12.

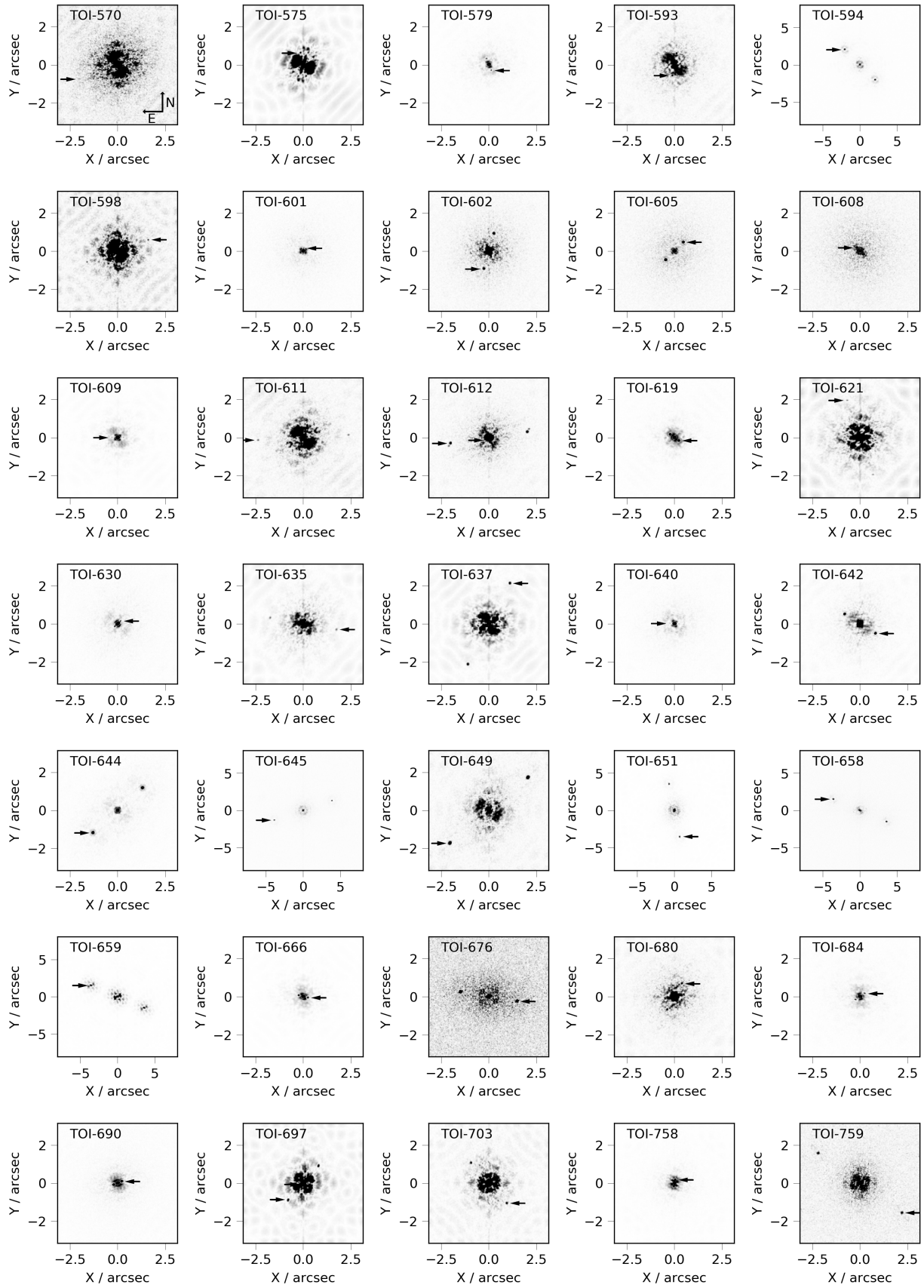

Figure 14. Similar to Figure 12.

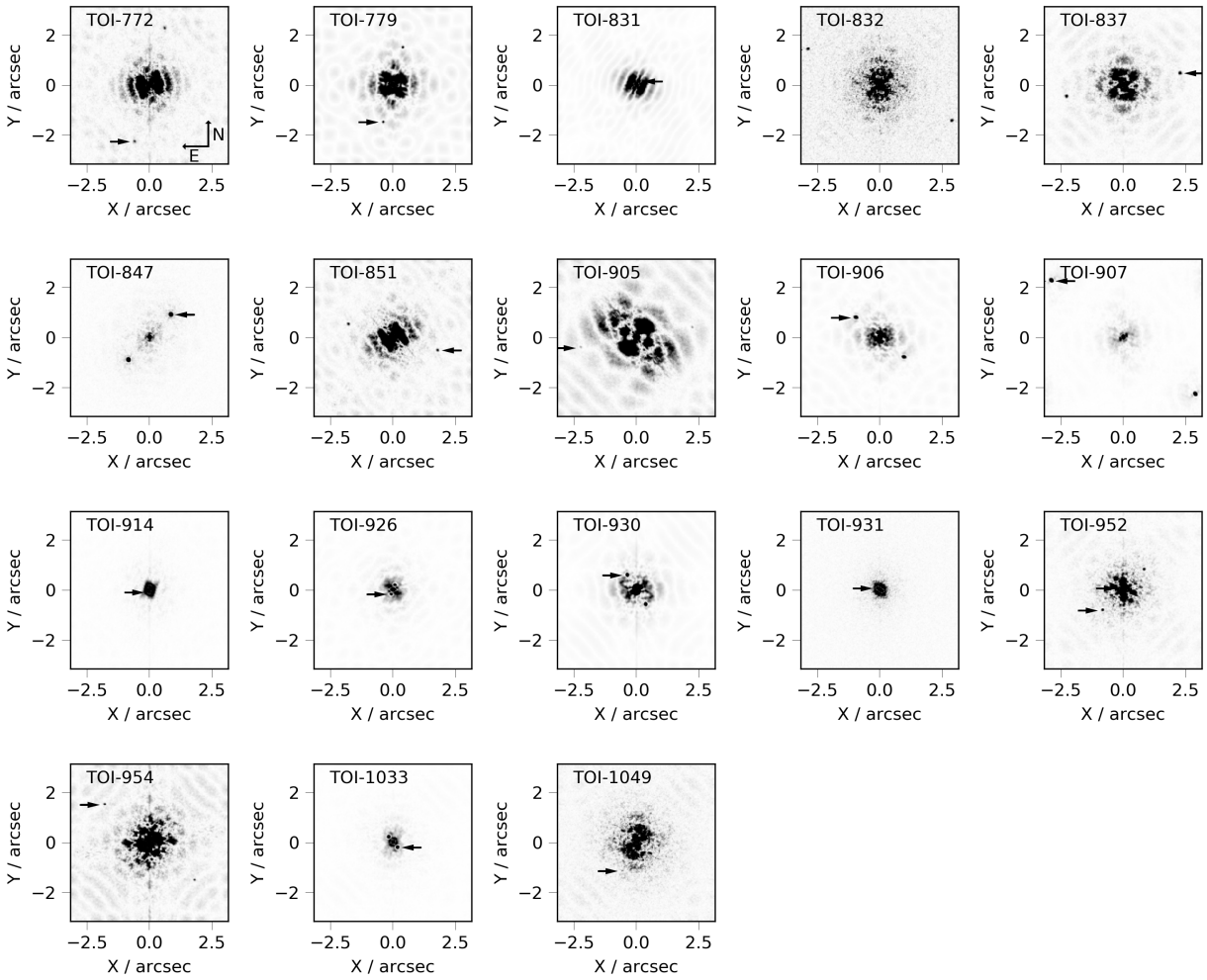

Figure 15. Similar to Figure 12.

Table 3. Gaia DR2 matches to resolved binaries detected by SOAR

TOI	TIC	Gaia DR2 IDs		SOAR			Gaia DR2		
		Primary	Secondary	Sep. (″)	P.A. (°)	Contrast (mag)	Sep. (″)	P.A. (°)	Contrast (mag)
123	290131778	6790773586275235200	6790773586276283648	1.2894	294.6	1.8	1.299	294.18	1.74
128	391949880	4621607053580909568	4621606297664620544	2.2195	153.8	2.4	2.2	153.78	2.55
147	220435095	4762555785607165824	4762555785606163712	2.6583	217.6	4.6	2.642	217.78	4.73
149	260985861	4621665155898448768	4621665155896340480	1.117	132.6	0.1	1.112	132.92	0.1
165	350743714	4765618612685018368	4765618681404494976	2.4855	254.5	0.8	2.476	254.49	0.81
180	51912829	4704412128965720448	4704412133261234176	1.2682	63.7	4.3	1.259	63.1	4.21
240	101948569	4982951791883929472	4982951791883929600	2.3656	197.6	3.1	2.347	197.72	3.44
245	154618248	6554931361478622976	6554931365773693952	1.6268	258.2	1.7	1.623	258.11	1.93
253	322063810	4928367189956040960	4928367189957786240	2.6623	351.2	4.0	2.639	351.78	4.13
258	350445771	4766550723668101376	4766550723668101248	2.0749	343.2	2.9	2.069	343.33	3.03
268	219253008	4779340346001388160	4779340277281911168	2.3025	51.2	0.3	2.29	51.36	0.2
343	66497310	2390762797648110336	2390762797648110208	2.8471	321.0	4.5	2.831	318.96	4.92
386	238059180	5497685201192526976	5497685205489860864	1.1739	274.4	3.5	1.151	268.65	3.54
387	92359850	5101513745613343232	5101513745612593536	2.2878	342.9	3.2	2.285	342.79	3.53
394	9858404	5167486711022397696	5167486711021821568	3.2284	220.2	3.8	3.221	219.92	3.59
427	70914192	5093541152441483008	5093541152441482880	2.6122	152.9	4.8	2.61	152.86	5.27
433	188989177	2983552564639203584	2983552603294316800	4.0098	324.5	2.9	3.984	324.61	3.13
494	19519368	3063507748837064064	3063507744545211264	2.2257	153.7	5.7	2.137	163.16	5.32
498	121338379	3071584413361857280	3071584417656749440	2.1845	251.5	3.5	2.251	252.84	3.52
594	146406806	5548005695180852352	5548005695180850816	2.8688	45.3	0.4	2.868	45.24	0.39
611	154459165	5693753348782558336	5693753348782877440	2.3787	93.3	5.5	2.378	93.73	5.67
635	286132427	3825847092208384640	3825847092207940736	1.7656	260.4	4.8	1.721	252.13	4.93
637	133334108	5537925196465380864	5537925200762994304	2.3926	332.9	5.1	2.393	332.43	5.02
644	63303499	2921445417696098944	2921445417696099072	1.758	132.4	0.4	1.753	132.52	0.39
645	157568289	5566329915436684672	5566329915435059712	4.0745	109.0	1.9	4.068	108.89	1.94
651	72090501	3004190986305089536	3004190986305090176	3.608	191.7	2.2	3.602	191.28	2.59
651	293689267	5568872394338114560	5568872398635858816	3.2615	219.3	1.5	3.344	219.25	1.58
658	48476907	5434682330226436480	5434682330226436736	3.88	67.2	0.7	3.877	67.14	0.75
659	48476908	5434682330226436480	5434682330226436736	3.8774	67.2	1.0	3.877	67.14	0.75
703	237928815	4680955147898508032	4680955152194431616	1.4153	221.8	4.7	1.415	221.71	5.0
759	152147232	5395959695358663296	5395959695358663040	2.694	234.6	3.6	2.687	234.81	3.75
772	286864983	3502914269362946688	3502914273658344448	2.3419	165.3	5.8	2.343	165.32	5.71
837	460205581	5251470948229949568	5251470948222139904	2.3128	281.7	4.6	2.312	281.52	4.7
847	231289421	4741068682700581376	4741068682699441280	1.2446	317.1	0.7	1.238	317.09	0.7
851	40083958	2426349694072115968	2426349694072132608	1.8583	253.8	5.2	1.849	253.86	5.52
905	261867566	5795534040654879744	5795534040654879488	2.2757	100.8	5.9	2.248	100.34	6.13
906	298372701	5984166216846046208	5984166221141887232	1.246	50.8	2.8	1.244	50.4	3.05
907	305424003	5910312231273215872	5910312231273215616	3.6665	52.0	1.1	3.648	52.0	1.11

Table 4. Gaia DR2 binaries to TESS targets not detected by SOAR

TOI	TIC	Gaia DR2 ID		Distance [9]		Proper motion		Sep.	Projected sep.	Gaia contrast
		Primary	Secondary	Primary	Secondary	Primary	Secondary			
				(pc)	(pc)	(mas/yr)	(mas/yr)	(″)	(AU)	(mag)
129	201248411	4923860051276772608	4923860051276772480	61.8	61.9	215.1	219.7	3.81	235.5	4.8
130	263003176	4617759514501503616	4617759518796452608	57.6	56.1	142.7	151.4	2.25	129.6	5.42
143	25375553	6813902839862151936	6813902839862983296	298.1	293.1	13.6	14.3	5.03	1499.4	5.02
174	425997655	4674216245427964416	4674216245427964672	39.0	39.2	111.6	111.5	9.57	373.2	6.45
183	183979262	4686544382117423488	4686544382117422720	213.0	215.4	79.4	80.4	3.21	683.7	2.63
199	309792357	4762582895440787712	4762582861080613248	102.3	101.8	74.2	73.4	9.99	1022.0	7.84
200	410214986	6387058411482257536	6387058411482257280	44.1	44.1	104.2	102.0	5.36	236.4	1.08
204	281781375	4903786336207800576	4903786336207800704	95.3	95.1	173.5	174.0	10.25	976.8	1.16
222	144440290	6531037981670835584	6531037981670835456	84.0	81.1	178.5	177.4	3.46	290.6	8.02
229	120610833	2308834780352875904	2308834784647991168	211.2	233.7	70.7	70.5	4.37	922.9	6.96
248	201793781	4743138925656526976	4743138925656526848	76.0	75.7	94.4	95.6	5.02	381.5	5.45
268	219253008	4779340346001388160	4779341750455118720	320.5	325.9	21.5	21.1	9.99	3201.8	8.13
277	439456714	2353440974955205504	2353440974955205632	64.7	64.7	273.5	274.6	17.25	1116.1	0.3
300	166697854	4743406244421179264	4743406244421179136	397.4	377.7	15.2	16.0	4.1	1629.3	4.66
354	100097716	4959658534969336320	4959658534969336576	366.8	404.5	28.6	28.5	4.84	1775.3	0.65
354	299780329	4632142191744789888	4632142196040368896	305.6	306.9	17.2	17.2	7.37	2252.3	3.25
368	77031413	2323985539482908416	2323985535188372480	233.0	233.6	88.4	87.9	6.12	1426.0	0.59
377	139285736	6529468772420035712	6529468772420035584	244.3	259.0	12.0	10.4	9.29	2269.5	3.14
381	207084429	4917040330405933824	4917040330405933952	75.5	82.3	152.9	156.8	4.94	373.0	7.62
390	250386181	2491782421314919040	2491782417019596160	167.3	171.3	38.4	38.2	6.28	1050.6	6.32
393	29960109	5157183324996790272	5157183324996789760	37.9	37.9	170.6	180.2	8.35	316.5	0.29
396	178155732	5064574720469473792	5064574724768583168	32.0	30.9	162.4	173.2	8.36	267.5	9.8
397	219379012	4785828357959075840	4785828357959076480	167.0	168.4	31.3	29.8	4.32	721.4	4.84
412	7624182	4844367147295252864	4844365669826503808	460.7	446.6	11.5	11.3	7.88	3630.3	6.0
414	325680697	5171630735987857152	5171630735987104512	115.1	114.8	48.3	48.6	4.5	517.9	5.25
426	189013224	2983316311375470976	2983316311375257472	113.6	112.6	26.2	27.8	8.88	1008.8	0.77
440	143350972	2971536418673198976	2971536418671276544	49.3	49.1	113.0	112.1	6.45	318.0	4.87
441	316916655	2987545475475708416	2987545548491503360	184.0	177.7	10.9	12.3	15.64	2877.8	6.0
470	37770169	2912264564319611136	2912264564316598272	130.5	130.1	85.1	84.4	13.6	1774.8	6.25
470	37770169	2912264564319611136	2912264564316598144	130.5	130.5	85.1	86.4	13.74	1793.1	5.89
498	121338379	3071584413361857280	3071584417656748928	188.4	176.6	23.4	21.7	5.2	979.7	7.25
505	268644785	5489780919480009472	5489780919477609600	324.7	315.8	5.1	5.4	6.09	1977.4	6.65
510	238086647	5508330367833229824	5508330367831469952	93.1	94.0	124.6	122.8	5.48	510.2	3.93
575	386435344	5709861464697757824	5709861468994311424	182.0	156.4	48.6	48.5	5.36	975.5	8.28

Table 4 – *Continued*

TOI	TIC	Gaia DR2 ID		Distance		Proper motion		Sep.	Projected sep.	Gaia contrast
		Primary	Secondary	Primary	Secondary	Primary	Secondary	(″)	(AU)	(mag)
580	81419525	5519619186857962112	5519619191155977344	346.5	475.4	11.6	9.1	14.09	4882.2	10.99
581	180987952	5525188767305211904	5525188728649771392	434.2	428.8	13.6	20.8	7.8	3386.8	8.56
592	196286587	5695996352497664512	5695996348197148032	358.4	385.6	8.6	33.0	11.28	4042.8	1.49
638	78154865	3822912388299321728	3822912392594624128	96.6	97.6	14.3	16.0	10.53	1017.2	4.32
648	78672342	2933433564771909888	2933433564771909760	637.3	814.6	11.0	11.6	2.95	1880.0	5.9
650	349373192	5293295919554813952	5293296130007438848	402.8	348.7	12.6	12.9	8.97	3613.1	8.93
670	147660201	5388433503908280320	5388433503908279168	191.5	183.6	57.9	56.4	13.79	2640.8	1.91
708	391821647	4657888149862830720	4657888150116259584	214.8	347.2	24.0	21.4	13.74	2951.4	9.36
756	73649615	6129327525817451648	6129327319659021056	86.2	86.2	218.3	217.6	11.09	956.0	1.35
764	181159386	5385762893242980992	5385762824520652160	789.3	754.5	6.5	6.4	5.96	4704.2	6.21
811	100757807	2890519660294945920	2890519660294833792	284.0	283.8	29.7	29.1	4.33	1229.7	1.83
815	102840239	5415648821879172096	5415648821874435584	59.7	59.3	11.4	12.3	6.04	360.6	2.48
824	193641523	5880886001621564928	5880886001577333888	63.9	69.2	160.9	3.3	6.7	428.1	9.16
829	276128561	6199033466340798464	6199033466344807040	142.5	138.8	71.0	71.4	5.46	778.0	5.28
832	350332997	4768613025228556416	4768613029524059648	586.7	617.2	13.7	12.9	3.7	2170.8	4.76
858	198008005	4683737294568479104	4683737294569921664	255.8	250.5	15.1	15.5	10.95	2801.0	0.28
878	219380235	4771537902252716416	4771537897957355392	334.5	324.6	35.5	34.9	5.64	1886.6	6.49
915	259389219	4781316164099781760	4781316168396825728	506.4	443.0	10.1	29.7	6.05	3063.7	4.18
938	332660150	3189432444744896512	3189432444743495936	215.0	195.0	12.6	12.9	7.95	1709.2	7.6

Table 5. Full SOAR Speckle Observation List and Binary Properties

TOI	TIC	R.A., Dec. (J2000) (deg)		Filter	Obs. Year	P.A. (°)	$\rho * \sigma_\theta$ (mas)	Sep. (″)	σ_{sep} (mas)	Delta Mag. (mag)	Min. Sep. (″)	Limiting Δm 0.″15	1″
101	231663901	318.73713	-55.87186	I	2018.731						0.067	2.20	2.97
109	29344935	313.21605	-25.68764	I	2019.375						0.098	0.00	0.00
112	388104525	55.93345	-65.19383	I	2019.534						0.064	2.33	3.88
114	25155310	63.37440	-69.22675	I	2019.534						0.064	2.51	4.37
118	266980320	349.56216	-56.90408	I	2018.731						0.048	3.00	4.05
119	278683844	99.23777	-58.01477	I	2018.732						0.048	2.36	3.72
120	394137592	4.44608	-66.35889	I	2018.731						0.043	2.57	3.82
121	207081058	331.86741	-41.81472	I	2018.731						0.052	2.33	3.67
122	231702397	332.94818	-58.94689	I	2018.975						0.041	1.68	3.86
123	290131778	319.69946	-26.61611	I	2018.731	294.6	0.2	1.289	0.2	1.8	0.041	2.42	4.38
123	290131778	319.69946	-26.61611	V	2018.731	294.6	0.3	1.292	0.2	1.8	0.064	2.13	2.81
123	290131778	319.69946	-26.61611	I	2019.375	294.6	0.1	1.286	0.1	1.8	0.041	2.39	4.88
124	29831208	66.58247	-67.80619	I	2018.805						0.064	2.22	3.77
125	52368076	23.59243	-66.67642	I	2018.731						0.052	2.69	4.15
126	70440470	339.48925	-35.15447	I	2018.731						0.064	2.03	2.77
128	391949880	79.52229	-80.96458	I	2018.732	40.3	3.2	1.534	3.2	5.1	0.046	2.57	3.53
128	391949880	79.52229	-80.96458	I	2018.806	153.8	0.4	2.220	2.3	2.4	0.064	2.34	4.39
129	201248411	0.18798	-54.83034	I	2018.731						0.048	2.64	3.98
130	263003176	12.53816	-83.74397	I	2018.731						0.043	2.53	4.38
131	235037761	353.83115	-64.56194	I	2018.731	205.6	1.4	0.076	1.9	1.2	0.051	2.35	3.59
131	235037761	353.83115	-64.56194	V	2018.731	198.0	5.2	0.075	4.5	1.8	0.063	2.37	2.68
131	235037761	353.83100	-64.56208	I	2018.805	207.1	0.3	0.076	2.0	1.1	0.054	2.40	3.72
131	235037761	353.82729	-64.56181	I	2019.534	246.1	2.0	0.033	2.1	1.0	0.056	2.68	3.96
132	89020549	338.39977	-43.43686	I	2018.731	334.8	4.1	0.080	3.6	2.6	0.046	2.29	3.88
132	89020549	338.39917	-43.43697	I	2019.375						0.041	2.96	4.84
133	219338557	354.39928	-58.95561	I	2018.731						0.048	2.59	3.89
134	234994474	350.03291	-60.06487	I	2018.731						0.048	2.47	4.04
135	267263253	7.32928	-76.30358	I	2018.731						0.046	2.80	4.25
136	410153553	340.49728	-69.17278	I	2018.731						0.057	2.38	3.07
137	176957796	101.29790	-66.23839	I	2018.732						0.056	2.23	3.46
138	277683130	328.92635	-61.67325	I	2018.731	256.3	0.1	0.097	1.7	1.1	0.052	2.12	3.39
138	277683130	328.92635	-61.67325	V	2018.731	256.1	0.7	0.101	0.8	1.1	0.058	2.08	3.09
138	277683130	328.92579	-61.67325	I	2018.805	257.0	1.0	0.096	0.2	1.2	0.053	2.09	3.69
138	277683130	328.92590	-61.67328	I	2019.375	258.0	0.5	0.099	0.7	1.2	0.041	1.53	4.89
139	62483237	336.40220	-34.90951	I	2018.731						0.046	2.44	3.97

Table 5 – *Continued*

TOI	TIC	R.A., Dec. (J2000) (deg)	(deg)	Filter	Obs. Year	P.A. (°)	$\rho * \sigma_\theta$ (mas)	Sep. (″)	σ_{sep} (mas)	Delta Mag. (mag)	Min. Sep. (″)	Limiting Δm 0.″15	1″
140	140068425	330.30183	-49.06011	I	2018.731						0.066	2.23	2.23
141	403224672	338.98517	-59.86426	I	2018.731	305.2	0.3	1.200	1.0	5.4	0.043	2.53	4.05
141	403224672	338.98517	-59.86426	I	2019.534	305.1	1.1	1.209	1.6	5.1	0.064	2.84	4.53
141	403224672	338.98517	-59.86426	I	2018.731	239.5	1.0	0.443	0.5	4.9	0.043	2.53	4.05
141	403224672	338.98517	-59.86426	I	2019.534	238.9	0.3	0.445	2.1	4.8	0.064	2.84	4.53
143	25375553	328.76728	-22.61306	I	2018.731						0.057	2.45	3.48
144	261136679	84.30888	-80.45922	I	2018.972						0.041	1.70	4.15
145	265612438	333.17453	-55.97869	I	2018.731						0.066	1.98	2.74
146	355636844	358.30280	-56.01356	I	2018.731	76.3	0.6	0.289	0.2	0.9	0.053	2.84	3.16
146	355636844	358.30280	-56.01356	V	2018.731	76.5	0.6	0.291	0.4	1.1	0.054	2.42	2.64
146	355636844	358.30280	-56.01314	I	2018.805	76.1	0.4	0.290	0.2	0.8	0.064	2.37	3.65
147	220435095	73.64068	-57.51286	I	2018.972	217.6	4.7	2.658	4.7	4.6	0.041	2.42	4.04
148	393940766	338.32068	-38.15925	I	2018.731						0.051	2.28	3.64
149	260985861	76.63612	-80.76825	I	2018.732	132.6	0.5	1.117	0.5	0.1	0.064	2.42	3.32
150	271893367	112.96512	-73.60619	I	2018.806						0.064	2.17	3.78
151	382302241	83.34938	-58.74497	I	2018.732						0.053	2.28	3.41
152	403287048	332.35713	-62.33500	I	2018.731						0.064	2.31	3.15
153	231081369	68.07354	-66.91622	I	2018.805	173.6	1.6	0.169	1.4	0.1	0.115	1.75	2.52
154	389525208	313.26174	-38.59489	I	2019.375						0.041	2.57	4.93
155	129637892	321.11500	-37.85008	I	2018.731						0.045	2.49	3.91
156	220518305	41.46797	-64.32039	I	2018.732						0.052	2.51	3.76
157	140691463	73.70170	-76.68056	I	2018.805						0.082	1.94	3.12
158	403136413	333.57863	-55.37883	I	2018.731						0.072	1.82	2.61
159	394657039	51.78245	-78.55025	I	2018.732	17.5	5.2	0.644	5.4	3.3	0.053	2.58	3.78
159	394657039	51.78208	-78.54983	I	2019.534	17.8		0.645	9.3	4.8	0.064	2.57	4.28
160	253917293	337.50114	-31.92436	I	2018.732						0.052	2.39	3.54
161	348770361	46.68695	-82.31636	I	2018.732	101.6	0.5	0.198	4.5		0.085	1.95	2.42
161	348770361	46.68695	-82.31650	I	2018.806	101.2	3.0	0.196	1.7		0.109	1.62	1.62
161	348770361	46.68609	-82.31611	I	2019.534	101.2	0.4	0.196	1.6		0.087	1.76	2.77
162	99493790	317.63979	-23.30592	I	2018.731						0.055	2.17	3.11
163	179317684	79.76814	-71.89544	I	2018.732						0.058	2.36	3.32
164	79395355	320.05428	-51.31003	I	2018.731						0.057	2.43	3.66
165	350743714	88.88621	-57.29056	I	2018.732	131.3	4.6	1.017	4.6	5.2	0.046	2.33	3.28
165	350743714	88.88621	-57.29056	I	2018.806	254.5	0.4	2.486	0.1	0.8	0.064	2.42	5.07
166	147203645	323.19643	-44.01806	I	2018.731						0.057	2.38	3.39

Table 5 – *Continued*

TOI	TIC	R.A., Dec. (J2000) (deg)	(deg)	Filter	Obs. Year	P.A. (°)	$\rho * \sigma_\theta$ (mas)	Sep. (″)	σ_{sep} (mas)	Delta Mag. (mag)	Min. Sep. (″)	Limiting Δm 0.″15	1″
167	149990841	90.66327	-64.81956	I	2018.732	308.0	4.6	0.172	1.1	1.1	0.068	2.04	2.09
167	149990841	90.66272	-64.81900	I	2018.806	306.6	2.8	0.159	8.8	0.8	0.107	1.72	2.45
167	149990841	90.66257	-64.81956	I	2019.134	307.6	1.6	0.168	0.2	1.0	0.064	2.04	3.85
168	369457671	311.64246	-37.90403	I	2018.731						0.052	2.21	3.24
169	183120439	16.77860	-75.19933	I	2018.731						0.061	2.27	3.31
170	394698182	54.99060	-83.08858	I	2018.732						0.070	2.26	3.06
171	309257814	124.26966	-63.21358	I	2018.806						0.075	2.29	3.45
172	29857954	316.63202	-26.69267	I	2018.731	319.0	5.2	1.104	5.2	4.9	0.052	2.48	3.01
172	29857954	316.63188	-26.69308	I	2018.805	319.1	2.8	1.102	2.9	4.9	0.064	2.10	4.44
172	29857954	316.63243	-26.69294	I	2019.375	319.7	5.4	1.121	13.1	3.5	0.041	2.22	4.50
173	270341214	33.45790	-80.58284	I	2018.972						0.041	2.48	4.63
174	425997655	55.46054	-62.76697	I	2018.805						0.050	2.42	4.41
175	307210830	124.53422	-68.31619	I	2018.806						0.064	2.54	4.21
176	272086159	115.00350	-72.20494	I	2018.975						0.046	1.67	3.42
177	262530407	20.43952	-46.71418	I	2018.805						0.064	2.18	4.20
178	251848941	7.30167	-30.45581	I	2018.805						0.064	2.49	4.31
179	207141131	44.26083	-56.21636	I	2018.806						0.048	2.40	3.78
179	207141131	44.26083	-56.21636	I	2018.972						0.041	2.61	5.07
179	207141131	44.26083	-56.21636	I	2019.134						0.064	2.90	4.85
180	51912829	14.29824	-67.49630	I	2018.972	63.7	2.3	1.268	2.6	4.3	0.041	1.96	4.31
180	51912829	14.29824	-67.49630	I	2019.534	63.6	1.8	1.267	3.2	4.2	0.064	2.16	3.49
181	76923707	352.17267	-34.49167	I	2018.975						0.041	2.65	5.56
182	76989773	353.29392	-35.46433	I	2018.975						0.041	2.92	5.59
183	183979262	21.65031	-72.74892	I	2018.972	98.5		0.083	1.4	0.4	0.041	0.00	4.35
183	183979262	21.65031	-72.74892	y	2018.972	97.7	0.1	0.088	2.2	0.3	0.033	1.57	4.35
183	183979262	21.64988	-72.74797	I	2019.534	97.5	0.2	0.094	0.4	0.5	0.064	2.11	3.83
183	183979262	21.65031	-72.74892	I	2018.972	302.0	0.4	3.181	1.0	5.1	0.041	0.00	4.35
183	183979262	21.64988	-72.74797	I	2019.534	301.8	0.4	3.184	0.1	3.3	0.064	2.11	3.83
184	300871545	117.65738	-70.53344	I	2018.975						0.041	2.03	4.81
186	279741379	51.74483	-63.49850	I	2018.972						0.041	2.78	5.25
187	260304296	94.61447	-57.01408	I	2018.972	104.5	2.2	0.846	1.1	2.1	0.041	2.19	4.67
188	280830734	44.55598	-70.76128	I	2018.972	5.8	2.3	1.290	2.3	4.8	0.041	2.60	4.83
189	278866211	100.80775	-55.24433	I	2018.972	341.7	1.3	0.972	1.3	4.1	0.041	1.96	4.43
193	183985250	358.66677	-37.62775	I	2018.975						0.041	2.53	5.40
196	234519192	14.55169	-64.76165	I	2018.972						0.041	2.52	4.72

Table 5 – *Continued*

TOI	TIC	R.A., Dec. (J2000) (deg)	(deg)	Filter	Obs. Year	P.A. (°)	$\rho * \sigma_\theta$ (mas)	Sep. (″)	σ_{sep} (mas)	Delta Mag. (mag)	Min. Sep. (″)	Limiting Δm 0.″15	1″
197	441462736	353.03389	-21.80154	I	2018.975						0.041	2.59	5.65
198	12421862	2.26627	-27.12235	I	2018.975						0.041	2.60	5.43
199	309792357	80.10595	-59.89536	I	2019.134						0.064	2.68	4.51
200	410214986	354.91396	-69.19559	I	2019.534						0.064	2.51	4.35
201	350618622	87.40169	-54.91087	I	2019.134						0.064	2.55	4.69
203	259962054	43.01792	-67.68686	I	2019.133						0.064	2.51	3.91
204	281781375	12.97547	-59.34317	I	2019.534						0.064	2.32	3.59
205	281575427	7.97529	-56.96508	I	2019.534						0.064	2.46	3.68
206	55650590	73.73845	-62.52175	I	2019.134						0.067	2.48	4.13
207	260271203	94.21809	-58.22981	I	2019.134						0.082	2.09	3.39
208	314865962	53.28162	-72.74400	I	2019.133						0.064	2.73	4.39
209	52204645	19.39457	-66.90289	I	2019.534						0.068	2.21	3.65
210	141608198	88.96212	-73.98542	I	2019.134						0.077	2.64	4.00
211	300293197	110.27972	-68.57836	I	2019.134	258.3	0.3	0.208	0.7	0.2	0.053	2.32	4.17
213	234345288	38.88745	-71.62428	I	2019.133						0.064	2.58	4.33
214	167415965	99.46183	-70.93334	I	2019.134						0.064	2.51	4.44
215	231912935	7.31808	-63.79061	I	2019.534						0.064	2.25	4.04
216	55652896	73.97995	-63.26039	I	2019.134						0.064	2.61	4.42
217	260043723	91.60875	-58.95372	I	2019.134						0.064	2.61	4.69
219	260609205	97.45388	-57.25481	I	2019.134						0.064	2.41	3.95
220	150098860	91.79967	-61.99728	I	2019.134						0.064	2.58	4.71
222	144440290	359.16095	-44.71890	I	2019.375						0.041	3.11	5.58
223	326453034	339.67734	-25.63231	I	2019.375						0.041	2.76	4.77
224	70797900	1.97754	-29.97914	I	2019.534	31.1	0.6	0.061	0.3	0.8	0.064	2.21	4.21
225	47525799	343.87992	-24.40964	I	2019.375						0.041	2.66	4.70
226	47484268	342.96714	-24.78758	I	2019.375						0.055	1.69	2.98
229	120610833	5.23746	-35.99828	I	2019.534						0.064	2.32	4.18
230	160074939	346.31904	-36.94547	I	2019.375						0.041	2.99	5.58
233	415969908	343.70828	-18.91228	I	2019.613						0.065	2.16	3.67
235	280095254	46.19617	-73.39656	I	2019.133	291.6	0.5	0.833	0.1	1.5	0.064	2.76	4.02
235	280095254	46.19617	-73.39656	I	2019.534	291.4	0.4	0.834	0.2	1.3	0.064	2.66	4.27
236	9727392	358.44420	-10.88469	I	2019.534						0.064	2.20	3.84
238	9006668	349.23102	-18.60664	I	2019.375						0.041	2.93	5.08
239	9725627	358.40826	-10.11836	I	2019.534						0.064	2.29	4.26
240	101948569	14.75480	-44.16111	I	2019.534	197.6	0.6	2.366	0.6	3.1	0.064	2.39	4.30

Table 5 – *Continued*

TOI	TIC	R.A., Dec. (J2000) (deg)	(deg)	Filter	Obs. Year	P.A. (°)	$\rho * \sigma_\theta$ (mas)	Sep. (″)	σ_{sep} (mas)	Delta Mag. (mag)	Min. Sep. (″)	Limiting Δm 0.″15	1″
242	120585579	4.45146	-38.11111	I	2019.534	164.3	0.5	0.823	0.9	2.0	0.064	2.19	3.63
243	149010208	3.39408	-31.33439	I	2019.534						0.064	2.31	3.97
244	118327550	10.56982	-36.71811	I	2019.534						0.064	2.45	4.46
245	154618248	345.77892	-33.50039	I	2019.375	258.1	0.1	1.627	0.2	1.7	0.041	2.96	5.11
245	154618248	345.77892	-33.50039	I	2019.534	258.2	0.8	1.618	1.0	2.0	0.064	2.86	4.54
248	201793781	34.68319	-54.85981	I	2019.134						0.064	2.85	4.75
249	179985715	14.08033	-38.94883	I	2019.534						0.064	2.49	4.46
251	224225541	353.06187	-37.25589	I	2019.375						0.041	3.00	5.39
252	237924601	57.55362	-63.05394	I	2019.134	311.5	1.1	0.419	0.4	1.5	0.075	2.39	3.68
252	237924601	57.55371	-63.05383	I	2019.534	310.7	0.7	0.420	0.7	1.5	0.086	1.94	3.23
253	322063810	14.31739	-51.58430	I	2019.534	351.2	1.0	2.662	1.3	4.0	0.064	2.15	3.68
254	49687222	351.70573	-11.72544	I	2019.375						0.041	2.99	5.14
256	92226327	11.24800	-15.27453	I	2019.534						0.064	2.11	3.91
257	200723869	47.51622	-50.83245	I	2019.134						0.040	2.73	4.76
258	350445771	85.46742	-56.74044	I	2019.134	343.2	0.6	2.075	1.0	2.9	0.064	2.40	4.41
260	37749396	4.77327	-9.96412	I	2019.613						0.064	2.48	4.63
261	63898957	15.21734	-24.42392	I	2019.534						0.064	2.30	4.65
262	70513361	32.53280	-31.06944	I	2019.133						0.064	2.61	4.83
264	122612091	41.04005	-30.16906	I	2019.537	331.5	1.8	0.641	1.8	4.5	0.064	2.47	4.77
265	159951311	49.56225	-41.30211	I	2019.537						0.064	2.57	4.48
266	164767175	26.20987	-18.40064	I	2019.537						0.064	2.21	3.75
268	219253008	65.91608	-53.85092	I	2019.134	51.2	1.0	2.303	0.4	0.3	0.064	2.56	4.93
269	220479565	75.84633	-54.17811	I	2019.134						0.064	2.28	4.05
270	259377017	68.41566	-51.95653	I	2019.614						0.064	2.93	4.94
271	259511357	70.77516	-50.21974	I	2019.134						0.064	2.66	4.89
273	279740441	51.50442	-64.54800	I	2019.134						0.064	2.58	4.26
274	281979481	130.50553	-75.80194	I	2019.134						0.064	2.86	4.04
275	373844472	81.51658	-67.23272	I	2019.134						0.064	2.54	4.48
276	382188882	81.35313	-55.01992	I	2019.134						0.064	2.35	4.55
277	439456714	19.07653	-20.95347	I	2019.613						0.065	2.07	3.86
279	122613513	41.18845	-32.21150	I	2019.133						0.064	2.62	4.61
280	42054565	24.16863	-36.41375	I	2019.534						0.064	2.30	4.40
281	38696105	66.13625	-60.12992	I	2019.134						0.064	2.75	4.74
282	29781292	65.23791	-68.10262	I	2019.134						0.064	2.93	4.76
283	382626661	118.56925	-65.44147	I	2019.134						0.064	2.52	4.48

Table 5 – *Continued*

TOI	TIC	R.A., Dec. (J2000) (deg)	(deg)	Filter	Obs. Year	P.A. (°)	$\rho * \sigma_\theta$ (mas)	Sep. (″)	σ_{sep} (mas)	Delta Mag. (mag)	Min. Sep. (″)	Limiting Δm 0.″15	1″
284	277103955	84.25434	-66.79072	I	2019.134						0.064	2.73	4.72
285	220459976	74.69717	-56.39375	I	2019.134						0.064	2.33	4.20
286	150030205	90.98442	-60.66633	I	2019.134						0.064	2.61	4.74
287	2758565	356.28285	-17.44950	I	2019.534						0.066	2.02	3.46
288	47316976	340.30743	-28.03300	I	2019.375						0.041	3.17	5.59
289	201292545	2.90031	-56.59964	I	2019.534						0.064	2.22	3.68
290	201233610	359.51650	-49.30083	I	2019.534						0.068	1.90	2.63
291	49710555	352.16469	-10.85986	I	2019.534						0.065	2.06	3.50
293	355637190	358.15446	-54.46889	I	2019.534	0.3	4.4	0.791	1.9	3.3	0.064	2.79	4.23
294	188570092	339.02649	-17.00031	I	2019.534						0.064	2.11	3.60
295	327952677	359.09151	-13.27133	I	2019.534	151.8	3.1	0.984	3.1	4.1	0.066	2.12	3.50
297	115242351	6.17691	-36.11442	I	2019.534						0.066	2.08	3.79
298	206686292	344.06072	-34.36139	I	2019.534						0.105	1.84	2.77
299	156075294	10.59462	-48.29386	I	2019.534						0.068	2.01	3.51
300	166697854	35.73774	-53.07006	I	2019.134						0.064	2.67	4.37
301	144301052	354.29747	-42.01028	I	2019.534						0.064	2.42	3.99
303	145750719	341.36405	-14.99178	I	2019.534						0.065	2.24	3.92
304	262530873	20.49377	-44.41647	I	2019.534						0.068	2.23	3.66
305	102030574	15.84467	-44.70581	I	2019.534						0.072	2.16	3.42
306	114749636	359.19126	-22.15319	I	2019.534						0.064	2.12	4.17
308	281710229	11.48466	-55.92264	I	2019.534	45.2	0.2	0.158	1.0		0.080	1.93	2.48
309	228507250	358.03959	-15.80083	I	2019.534	77.9	0.3	0.327	1.1	0.9	0.069	2.08	3.36
310	175477257	351.10500	-36.97572	I	2019.614						0.064	2.13	4.06
311	434105231	354.33531	-13.45569	I	2019.534						0.068	2.12	3.29
312	180145006	14.52357	-37.94225	I	2019.534						0.064	2.18	3.96
313	9102327	350.77952	-19.41911	I	2019.534						0.064	2.25	4.23
314	316769613	354.66825	-32.86092	I	2019.375						0.041	2.64	4.50
315	66356824	12.07602	-32.11967	I	2019.534						0.064	2.26	3.68
317	402319411	353.54008	-14.85969	I	2019.534						0.064	2.02	3.20
320	188593930	345.52270	-16.36014	I	2019.534						0.066	2.09	3.31
322	198077394	63.82521	-56.25367	I	2019.134	126.5	0.8	0.176	0.2	0.7	0.064	2.05	4.24
322	198077394	63.82490	-56.25375	I	2019.534	126.1	0.2	0.175	0.1	0.7	0.064	2.03	4.27
325	66413476	13.87733	-33.51250	I	2019.534	222.2	3.9	0.581	10.5	4.0	0.064	2.22	3.98
326	144336525	356.11488	-46.86658	I	2019.534						0.064	2.60	4.30
327	206669860	343.63303	-34.50272	I	2019.534						0.098	1.50	2.47

Table 5 – *Continued*

TOI	TIC	R.A., Dec. (J2000) (deg)	(deg)	Filter	Obs. Year	P.A. (°)	$\rho * \sigma_\theta$ (mas)	Sep. (″)	σ_{sep} (mas)	Delta Mag. (mag)	Min. Sep. (″)	Limiting Δm 0.″15	1″
329	169765334	351.32124	-15.63464	I	2019.375						0.041	2.70	4.58
331	262531275	20.41929	-42.48175	I	2019.534						0.072	2.04	3.34
332	139285832	348.05878	-44.87636	I	2019.534						0.064	2.59	4.30
333	224245334	353.35750	-41.17150	I	2019.375						0.041	2.66	4.17
334	233964642	36.49870	-63.64761	I	2019.134						0.064	2.74	4.56
335	41865539	21.32229	-39.94811	I	2019.534						0.064	2.31	3.84
336	55452495	70.67025	-64.88522	I	2019.134						0.064	2.59	4.64
337	155986102	7.32996	-50.14011	I	2019.534	60.8	6.5	0.145	22.0	2.0	0.066	1.95	3.23
338	116156517	7.70937	-40.57344	I	2019.534						0.064	2.46	4.19
339	69838258	337.92130	-21.94625	I	2019.375						0.046	2.11	3.27
340	80439101	11.74734	-44.36994	I	2019.534	338.0	4.5	0.237	3.3	1.8	0.072	1.94	3.27
343	66497310	356.04534	-18.88981	I	2019.534	319.0	5.4	2.847	5.4	4.5	0.066	2.12	3.47
344	13023378	347.05362	-28.00789	I	2019.375						0.041	2.50	3.70
346	118327533	10.34450	-37.34300	I	2019.534	285.3	15.0	1.433	15.0	5.6	0.068	2.24	3.96
347	224271611	354.48955	-36.57158	I	2019.375						0.041	2.67	4.31
348	70785910	1.58362	-30.33658	I	2019.534	40.8	6.8	1.396	6.8	4.8	0.064	2.22	3.98
350	199731190	21.29200	-47.26292	I	2019.534						0.064	2.34	3.83
351	228381868	357.58026	-17.07758	I	2019.534						0.064	2.14	3.90
352	47423120	342.06750	-24.83892	I	2019.375						0.041	2.65	4.42
354	100097716	24.04775	-42.30378	I	2019.534						0.064	2.15	3.94
355	183593642	17.88808	-36.70911	I	2019.534						0.064	2.52	4.13
356	369336146	6.06996	-37.22206	I	2019.534						0.064	2.20	3.94
357	220016044	32.32220	-48.48461	I	2019.134						0.064	2.68	4.29
358	321982642	3.06100	-47.35542	I	2019.534						0.068	1.91	2.98
359	80432617	11.67340	-42.36147	I	2019.534						0.064	2.53	3.99
360	13023738	347.08492	-29.59050	I	2019.534						0.070	2.36	3.80
361	144276942	353.90345	-44.80853	I	2019.534						0.064	2.48	4.04
363	262530780	20.54728	-44.86200	I	2019.534						0.072	2.07	3.45
364	47425697	342.25613	-24.95928	I	2019.375	96.0	0.5	0.374	0.3		0.041	2.46	3.99
365	118586896	10.92234	-38.04317	I	2019.534						0.068	2.12	3.67
367	9033144	349.60622	-19.82392	I	2019.375						0.041	2.87	5.04
368	77031413	354.17053	-34.61211	I	2019.375						0.041	2.35	3.90
369	175482273	351.22917	-38.16069	I	2019.375	139.3	0.3	0.695	0.1	1.2	0.041	3.00	4.93
371	156016136	8.92387	-50.31697	I	2019.534						0.072	1.96	3.34
372	441075486	359.75904	-15.61172	I	2019.534	260.6	0.9	0.239	2.6	2.6	0.064	2.07	3.93

Table 5 – *Continued*

TOI	TIC	R.A., Dec. (J2000) (deg)	(deg)	Filter	Obs. Year	P.A. (°)	$\rho * \sigma_\theta$ (mas)	Sep. (″)	σ_{sep} (mas)	Delta Mag. (mag)	Min. Sep. (″)	Limiting Δm 0.″15	1″
373	9032368	355.90188	-11.26953	I	2019.534						0.067	2.12	3.14
375	280097543	47.14988	-77.38333	I	2019.133						0.064	2.78	4.01
376	144301273	354.44562	-42.96639	I	2019.534						0.064	2.35	4.08
377	139285736	348.03980	-45.01683	I	2019.534						0.064	2.55	4.20
378	20892672	1.39928	-19.48894	I	2019.534	330.0	2.7	0.184	2.4	1.6	0.100	1.85	3.29
378	20892672	1.39928	-19.48894	I	2019.534	312.3	0.5	3.311	0.9	1.5	0.100	1.85	3.29
378	20892672	1.39928	-19.48894	I	2019.534	312.3	0.9	3.309	2.3	1.2	0.100	1.85	3.29
379	220396259	68.89158	-56.13872	I	2019.199	28.8	2.8	0.031	2.4		0.069	2.52	4.14
379	220396259	68.89153	-56.13875	I	2019.534	27.6	0.8	0.041	0.3		0.053	2.59	3.97
381	207084429	22.75606	-51.21526	I	2019.534						0.064	2.45	4.46
382	229091748	3.79775	-46.27242	I	2019.534						0.070	1.93	3.15
383	167418898	99.60963	-67.65631	I	2019.134	333.6	1.4	0.267	1.0	1.5	0.064	2.64	4.57
385	300810086	116.81330	-69.03031	I	2019.134						0.064	2.64	4.28
386	238059180	104.13834	-53.54544	I	2019.134	274.4	0.6	1.174	1.2	3.5	0.064	2.46	4.26
387	92359850	52.23087	-19.97461	I	2019.133	342.9	1.0	2.288	0.4	3.2	0.064	2.37	3.76
387	92359850	52.23087	-19.97461	I	2019.537	342.9	0.2	2.291	0.2	3.2	0.063	2.07	5.60
389	271900960	112.94194	-75.52736	I	2019.134						0.064	2.59	4.02
390	250386181	30.11450	-4.98572	I	2019.133						0.064	2.57	3.86
392	328350926	46.93172	0.86083	I	2019.133						0.064	2.59	3.53
393	29960109	42.25025	-14.53761	I	2019.133						0.064	2.55	4.08
394	9858404	48.49954	-8.57358	I	2019.133	220.2	0.9	3.228	1.1	3.8	0.064	2.95	4.56
395	38541473	56.30466	-10.97347	I	2019.133						0.052	2.77	3.78
396	178155732	42.98401	-30.81478	I	2019.133						0.064	2.59	4.72
397	219379012	76.83358	-48.11589	I	2019.134						0.064	2.39	4.56
399	219388773	77.04759	-50.85894	I	2019.134						0.064	2.52	4.48
401	259701242	74.46650	-53.81797	I	2019.134						0.064	2.50	4.77
402	120896927	36.86844	-27.63469	I	2019.537	233.4	2.1	1.439	2.1	5.2	0.064	2.38	4.86
405	176984236	101.90950	-66.32831	I	2019.134	321.5	0.5	0.386	0.2	0.9	0.064	2.60	3.93
406	153065527	49.26243	-42.24442	I	2019.133						0.064	2.63	4.70
407	349518800	111.21198	-62.09186	I	2019.134						0.068	2.30	3.81
408	176778112	47.82725	-35.62781	I	2019.133						0.064	2.58	4.88
409	167754523	104.18163	-60.68697	I	2019.134						0.064	2.61	4.62
410	206466531	56.81496	-52.98536	I	2019.134						0.064	2.61	4.91
411	100990000	54.82001	-42.76228	I	2019.134						0.064	2.73	4.73
412	7624182	64.31139	-38.84417	I	2019.134						0.043	2.62	4.85

Table 5 – *Continued*

TOI	TIC	R.A., Dec. (J2000) (deg)	(deg)	Filter	Obs. Year	P.A. (°)	$\rho * \sigma_\theta$ (mas)	Sep. ($''$)	σ_{sep} (mas)	Delta Mag. (mag)	Min. Sep. ($''$)	Limiting Δm $0\farcs15$	$1''$
414	325680697	36.85362	-12.03892	I	2019.133						0.064	2.57	4.12
415	152476657	62.61609	-45.89822	I	2019.537	89.6	3.2	2.230	3.2	4.8	0.064	2.50	4.60
416	49899799	48.85470	-2.17519	I	2019.133						0.064	2.73	3.86
417	339733013	110.85175	-58.69672	I	2019.134						0.064	2.47	4.32
419	279251651	104.15594	-59.18437	I	2019.134						0.064	2.45	4.34
420	408159788	78.44740	7.05600	I	2019.199						0.071	2.70	3.91
421	94986319	81.85341	-14.27689	I	2019.199						0.069	2.42	3.85
422	117979455	71.80308	-17.25314	I	2019.199	118.8	4.7	1.404	4.2	4.5	0.064	3.13	4.78
424	117979694	71.92134	-17.74453	I	2019.199						0.064	2.87	4.14
425	169532369	78.09897	-13.60522	I	2019.199						0.112	1.67	2.45
426	189013224	79.10222	-15.51014	I	2019.199						0.066	2.74	4.28
427	70914192	64.65639	-17.41986	I	2019.199	152.9	6.8	2.612	6.8	4.8	0.064	2.96	4.19
428	117979850	71.81020	-17.24842	I	2019.199						0.064	2.96	4.70
429	259592689	72.97700	-53.83036	I	2019.199						0.064	2.64	4.33
430	459942762	60.27816	4.54129	I	2019.619						0.075	2.29	3.87
431	31374837	83.26912	-26.72489	I	2019.199						0.064	3.02	4.67
432	38686737	57.86484	-10.61489	I	2019.199						0.111	1.79	2.36
433	188989177	78.77837	-15.10044	I	2019.199						0.063	2.87	5.40
433	188989177	78.77837	-15.10044	I	2019.204	324.5	2.8	4.010	3.4	2.9	0.063	2.87	5.40
435	44647437	59.41018	-25.18856	I	2019.199						0.121	1.60	2.44
440	143350972	82.24658	-17.42906	I	2019.199						0.064	3.19	4.81
441	316916655	74.47293	-13.70342	I	2019.199						0.064	3.02	4.46
442	70899085	64.19004	-12.08503	I	2019.199						0.069	2.55	3.84
444	179034327	64.18419	-26.76562	I	2019.537						0.064	2.25	4.55
445	14091704	77.32345	-36.59100	I	2019.199						0.064	2.95	4.54
446	1449640	75.17163	-35.20261	I	2019.199						0.097	1.83	2.90
447	14091633	77.26022	-36.46456	I	2019.199						0.064	2.96	4.54
450	77951245	79.00487	-31.41256	I	2019.199						0.087	2.00	3.14
451	257605131	62.96642	-37.93978	I	2019.199						0.064	2.81	4.17
454	153077621	49.66163	-42.64211	I	2019.199	256.7	1.0	3.868	0.8	2.2	0.064	2.80	4.87
455	98796344	45.46283	-16.59186	I	2019.614	317.5		1.033	0.3	0.7	0.064	2.47	4.19
458	64071894	39.13620	-22.24425	I	2019.537						0.064	2.28	4.64
459	38603673	64.41497	-61.39208	I	2019.199						0.064	2.62	4.35
461	4646810	38.27244	-10.35156	I	2019.537						0.064	2.40	4.52
462	420049884	36.27633	1.32394	I	2019.537	196.1	0.3	0.167	0.7	0.3	0.064	2.04	3.67

Table 5 – *Continued*

TOI	TIC	R.A., Dec. (J2000) (deg)	(deg)	Filter	Obs. Year	P.A. (°)	$\rho * \sigma_\theta$ (mas)	Sep. (″)	σ_{sep} (mas)	Delta Mag. (mag)	Min. Sep. (″)	Limiting Δm 0.″15	1″
463	176831592	48.95672	-32.80189	I	2019.199	215.0	2.2	0.808	2.2	3.5	0.064	2.87	4.37
463	176831592	48.95700	-32.80244	I	2019.537	214.8	0.5	0.805	0.9	3.6	0.064	2.45	4.57
467	20178111	89.89750	-40.39619	I	2019.199						0.064	2.85	4.59
469	33692729	93.05840	-14.65041	I	2019.199						0.064	3.21	4.60
470	37770169	94.00971	-25.03119	I	2019.199						0.064	2.82	4.34
472	52280468	99.86728	-33.54028	I	2019.199						0.079	2.14	3.46
475	100608026	86.74809	-32.53294	I	2019.199						0.064	2.62	4.41
476	156987351	99.58142	-47.61386	I	2019.199	145.4	10.0	0.657	6.1	4.6	0.064	2.73	4.40
476	156987351	99.58142	-47.61386	I	2019.377	146.0	3.5	0.652	1.9	4.5	0.041	2.90	5.32
478	172464366	100.15884	-27.57139	I	2019.199						0.064	2.57	4.16
480	317548889	88.37876	-16.26479	I	2019.199						0.064	3.22	4.69
481	339672028	110.51255	-57.38489	I	2019.199						0.064	2.92	4.40
484	427348923	83.53195	-0.20742	I	2019.199						0.068	2.51	3.75
485	427352241	83.62303	-4.41492	I	2019.199						0.066	2.76	4.22
487	31852980	52.53983	-70.39967	I	2019.534	201.0	0.2	0.511	0.2	1.2	0.064	2.54	3.67
487	31852980	52.53983	-70.39967	I	2019.534	130.2	0.1	2.993	0.1	5.1	0.064	2.54	3.67
494	19519368	124.69547	-6.78589	I	2019.377	153.6	7.7	2.226	7.7	5.7	0.041	2.46	5.14
498	121338379	129.09087	-3.86022	I	2019.377	251.4	0.9	2.185	0.9	3.5	0.041	2.74	5.00
499	123702439	115.63880	-43.55319	I	2019.377						0.041	2.75	5.15
500	134200185	106.55774	-47.58683	I	2019.377						0.041	2.97	5.29
501	134537478	108.30145	-42.40975	I	2019.377						0.041	2.81	5.00
502	172193428	98.53200	-28.40419	I	2019.377						0.041	2.55	4.73
505	268644785	117.41532	-52.12044	I	2019.377						0.041	2.56	4.74
510	238086647	104.95797	-49.50699	I	2019.377						0.041	2.91	5.48
512	119292328	96.64695	-38.60742	I	2019.377						0.041	2.77	5.15
520	148479278	102.65800	-37.96022	I	2019.377						0.041	2.65	5.25
522	19451711	124.60291	-7.57131	I	2019.377	241.0	1.7	0.753	1.7	4.9	0.041	2.76	5.53
525	71512186	90.16963	-8.46814	I	2019.377						0.041	2.83	5.12
527	148228019	101.18875	-36.65739	I	2019.377	255.8	0.4	0.221	0.2	2.1	0.041	2.20	4.97
533	309791156	80.05448	-62.64636	I	2019.537						0.064	2.46	4.73
540	200322593	76.30944	-47.93733	I	2019.537						0.064	2.26	4.44
550	311183180	55.03191	5.87458	I	2019.619	116.1	4.6	0.601	1.4	1.7	0.107	1.79	2.82
553	161477033	73.26132	-45.53978	I	2019.537						0.064	2.50	4.74
554	407966340	60.74772	9.20888	I	2019.619						0.069	2.29	4.12
557	55488511	59.01733	-10.27119	I	2019.537						0.064	2.08	3.94

Table 5 – *Continued*

TOI	TIC	R.A., Dec. (J2000) (deg)	(deg)	Filter	Obs. Year	P.A. (°)	$\rho * \sigma_\theta$ (mas)	Sep. (″)	σ_{sep} (mas)	Delta Mag. (mag)	Min. Sep. (″)	Limiting Δm 0.″15	1″
558	207110080	42.29150	-58.02467	I	2019.134						0.064	2.72	4.40
559	209459275	46.81858	-31.16306	I	2019.133						0.064	2.68	4.71
560	101011575	129.68874	-13.25679	I	2019.377						0.041	2.59	5.38
561	377064495	148.18573	6.21631	I	2019.377						0.041	2.01	4.76
563	405454160	143.24337	-17.34350	I	2019.377	33.3	0.3	0.384	0.1	0.8	0.041	2.04	4.58
564	1003831	130.29516	-16.03600	I	2019.377						0.041	2.53	5.06
568	37575651	135.34050	-28.32458	I	2019.377	190.6	0.1	0.295	0.3	0.8	0.041	1.53	4.81
569	123482865	115.10331	-42.15492	I	2019.377						0.041	2.79	5.37
570	126733133	136.95525	-51.86711	I	2019.374	110.5	27.4	2.164	27.4	6.6	0.041	2.23	4.66
575	386435344	127.99522	-16.88481	I	2019.377	13.8	1.8	0.629	2.7	4.7	0.041	2.87	5.44
579	238061845	104.12153	-50.15764	I	2019.377	202.5	2.7	0.330	1.1	3.3	0.041	2.56	5.04
580	81419525	123.10828	-46.10917	I	2019.377						0.041	2.84	5.42
581	180987952	130.26178	-41.44281	I	2019.374						0.041	2.73	4.80
582	287474726	127.12809	-28.35928	I	2019.377						0.041	2.59	5.41
583	131743355	118.47669	-39.99275	I	2019.377						0.041	2.83	5.44
584	74482749	137.51841	-43.92497	I	2019.374						0.041	2.82	5.04
585	190990336	134.37314	-39.77843	I	2019.374						0.041	2.91	5.32
586	131979339	118.91391	-37.85744	I	2019.377						0.041	2.97	5.63
587	294090620	130.39610	-22.19434	I	2019.377						0.041	2.47	5.42
588	130415266	104.74995	-47.02334	I	2019.377						0.041	3.02	5.66
589	412961700	127.22262	-20.95036	I	2019.377						0.041	2.59	5.58
591	146261607	123.58191	-34.81933	I	2019.377						0.041	2.77	5.09
592	196286587	125.55713	-25.06944	I	2019.377						0.041	2.28	5.18
593	128463355	118.05958	-29.71403	I	2019.377	169.6	3.2	0.579	3.0	3.9	0.041	2.62	4.88
594	146406806	123.73354	-31.60833	I	2019.377	45.2	1.1	2.869	1.0	0.4	0.041	2.28	4.56
595	287329267	109.78359	-59.30203	I	2019.377						0.041	2.69	5.12
596	144956678	122.06862	-35.55947	I	2019.377						0.041	2.51	5.18
597	146208651	133.45803	-48.81264	I	2019.374						0.041	2.31	4.94
598	81429971	123.17793	-42.93500	I	2019.377	290.4	10.4	1.711	10.4	6.2	0.041	2.63	5.40
599	145982812	133.14525	-50.00883	I	2019.374						0.041	2.38	4.54
600	134396419	122.27268	-37.06158	I	2019.377						0.041	2.52	5.15
601	141363913	129.46233	-43.04231	I	2019.374	352.4	3.4	0.151	6.6	3.1	0.041	2.55	4.41
602	175176327	115.82533	-36.49675	I	2019.377	164.3	1.6	0.976	1.6	3.7	0.041	2.85	5.08
603	262746281	141.10795	5.76619	I	2019.377						0.041	1.84	4.70
604	145027461	122.25750	-30.78794	I	2019.377						0.041	2.47	4.94

Table 5 – *Continued*

TOI	TIC	R.A., Dec. (J2000) (deg)	(deg)	Filter	Obs. Year	P.A. (°)	$\rho * \sigma_\theta$ (mas)	Sep. (″)	σ_{sep} (mas)	Delta Mag. (mag)	Min. Sep. (″)	Limiting Δm 0.″15	1″
605	181304295	130.91967	-36.65703	I	2019.374	315.4	0.5	0.655	2.3	1.1	0.042	2.00	3.31
606	122262940	133.23848	-57.94061	I	2019.377						0.041	2.42	4.82
607	153651591	121.00929	-26.16569	I	2019.377						0.041	2.59	4.91
608	186547153	132.83887	-34.43186	I	2019.374	44.3	2.0	0.248	0.9	0.1	0.045	1.20	3.03
609	134404603	122.34017	-39.16483	I	2019.377	91.0	1.3	0.300	2.8	4.0	0.041	2.70	5.23
610	80275202	121.52625	-44.37508	I	2019.377						0.041	2.62	4.88
611	154459165	122.03447	-28.06611	I	2019.377	93.2	7.8	2.379	7.8	5.5	0.041	2.18	4.79
612	284738182	110.88192	-37.83553	I	2019.377	98.6	0.7	2.025	1.8	3.9	0.041	2.97	5.00
612	284738182	110.88192	-37.83553	I	2019.377	145.1	1.6	0.173	0.7	1.5	0.041	2.97	5.00
613	77527511	142.26291	-5.37556	I	2019.377						0.041	1.92	5.01
614	118021229	128.47502	-20.94117	I	2019.377						0.041	2.79	5.21
615	190496853	133.40903	-40.54375	I	2019.374						0.041	2.61	4.28
616	145879095	132.87400	-51.32822	I	2019.374						0.041	2.20	4.72
617	141227133	129.31487	-47.38272	I	2019.377						0.041	2.49	5.02
618	173640199	112.57067	-39.33958	I	2019.377						0.041	2.76	5.24
619	267527924	114.05072	-48.06350	I	2019.377	234.5	0.1	0.280	0.1	1.0	0.041	1.83	4.60
621	30828562	134.71861	-43.45293	I	2019.374	19.1	10.6	2.065	10.6	6.5	0.041	2.55	5.41
622	83092282	125.30508	-46.48422	I	2019.377						0.041	3.01	5.60
623	101395259	148.72120	-23.32992	I	2019.374						0.041	2.39	4.65
626	65412605	108.12312	-24.95358	I	2019.377						0.041	2.83	4.94
630	123898871	90.91600	-19.04003	I	2019.377	315.7	2.8	0.210	5.5	3.6	0.041	1.88	4.45
631	97158538	105.94527	-30.72614	I	2019.377						0.041	3.03	5.32
634	344926234	151.55833	3.94681	I	2019.377						0.041	2.14	4.98
635	286132427	146.72484	-4.29797	I	2019.374	260.3	5.3	1.766	5.3	4.8	0.041	2.54	5.44
637	133334108	120.78738	-38.74167	I	2019.377	332.8	2.6	2.393	2.6	5.1	0.041	2.49	5.27
638	78154865	147.86650	-4.12389	I	2019.374						0.041	2.56	5.33
640	147977348	99.73487	-36.64617	I	2019.377	85.1	6.5	0.250	4.5	4.8	0.041	2.61	4.87
642	79292541	104.05580	-20.05194	I	2019.377	237.9	0.5	0.951	1.3	2.6	0.041	2.88	5.04
644	63303499	104.92288	-24.88408	I	2019.377	132.3	0.1	1.758	0.6	0.4	0.041	2.77	4.45
645	157568289	106.76798	-36.77083	I	2019.377	108.9	0.6	4.075	1.3	1.9	0.041	2.49	4.56
646	238197709	57.26559	-72.94739	I	2019.534						0.064	2.65	4.28
648	78672342	103.00251	-18.95444	I	2019.377						0.041	2.71	5.06
649	35582553	102.22243	-13.52783	I	2019.377	130.2	1.0	2.678	1.0	3.2	0.041	2.60	4.87
650	349373192	110.26104	-60.15550	I	2019.377						0.041	2.64	4.93
651	72090501	92.10579	-11.14628	I	2019.377	191.6	2.2	3.608	6.9	2.2	0.041	2.79	5.64

Table 5 – *Continued*

TOI	TIC	R.A., Dec. (J2000) (deg)	(deg)	Filter	Obs. Year	P.A. (°)	$\rho * \sigma_\theta$ (mas)	Sep. (″)	σ_{sep} (mas)	Delta Mag. (mag)	Min. Sep. (″)	Limiting Δm 0.″15	1″
652	22221375	149.12482	-24.09950	I	2019.374						0.041	2.73	5.67
653	33153766	144.77375	-45.42622	I	2019.374						0.041	2.51	5.41
657	48103627	147.40647	-33.21878	I	2019.533						0.093	1.78	2.86
658	48476907	150.15292	-34.68197	I	2019.374	247.1	0.6	3.880	0.9	-0.7	0.041	2.45	4.32
659	48476908	150.15292	-34.68197	I	2019.377	67.1	0.5	3.877	0.2	1.0	0.041	1.65	4.31
659	48476908	150.15292	-34.68197	I	2019.533	67.0	0.6	3.894	1.4	0.7	0.063	2.46	5.09
662	54085154	160.18022	-31.92717	I	2019.374						0.041	2.83	5.52
663	54962195	160.06547	-8.51164	I	2019.533						0.068	2.27	3.82
664	55092869	161.70745	-9.39884	I	2019.374						0.041	2.43	5.56
665	73723286	155.63691	-40.51619	I	2019.374						0.041	3.05	5.23
666	82128636	124.11042	-46.42989	I	2019.377	257.3	0.8	0.248	0.4	2.8	0.041	2.37	5.36
668	102195674	154.19184	-42.55903	I	2019.374						0.049	1.91	3.44
669	124573851	158.90034	-5.18131	I	2019.374						0.041	2.12	4.57
670	147660201	163.90933	-42.84933	I	2019.533						0.086	2.19	3.34
671	151681127	166.88900	-40.20694	I	2019.374						0.041	2.65	5.22
672	151825527	167.99050	-39.32789	I	2019.533						0.064	2.18	3.83
673	151959065	168.99850	-36.45942	I	2019.533						0.064	2.06	3.64
674	158588995	164.58722	-36.85808	I	2019.533						0.067	2.20	3.69
676	219187649	171.20604	-18.61731	I	2019.533	260.6	4.1	1.502	1.9	1.5	0.115	1.62	2.43
677	280206394	144.11978	-50.46353	I	2019.374						0.041	2.26	5.00
678	294395926	109.33116	-55.59842	I	2019.377						0.041	2.66	4.44
679	308050066	155.43600	-17.22439	I	2019.374						0.041	2.58	4.79
680	335499997	179.16399	-12.37746	I	2019.374	330.9	2.6	0.781	2.6	4.3	0.041	2.72	5.08
680	335499997	179.16399	-12.37746	I	2019.533	330.8	1.2	0.779	1.7	4.3	0.064	2.41	4.98
681	410450228	117.89496	-60.41217	I	2019.377						0.041	2.40	4.67
682	429304876	167.88463	-22.07289	I	2019.374						0.041	3.07	5.30
684	462162948	150.43367	-59.85003	I	2019.374	303.2	1.4	0.297	4.4	3.1	0.041	1.75	4.62
684	462162948	150.43371	-59.85031	I	2019.533	302.4	3.3	0.296	2.0	3.1	0.064	2.85	4.35
685	281731203	163.03237	0.49331	I	2019.533						0.064	2.32	4.24
686	339857675	111.60137	-54.45242	I	2019.377						0.041	2.76	5.04
688	339636032	110.19445	-55.37967	I	2019.377						0.041	3.00	5.51
689	445822015	147.00572	-48.32083	I	2019.374						0.042	1.99	3.69
690	101497191	149.22603	-33.79936	I	2019.374	292.3	0.7	0.222	0.3	1.2	0.041	2.00	4.27
690	101497191	149.22547	-33.79964	I	2019.533	292.3	0.7	0.219	1.6	1.1	0.066	2.01	3.72
694	55383975	77.38355	-64.02644	I	2019.534						0.064	2.51	4.09

Table 5 – *Continued*

TOI	TIC	R.A., Dec. (J2000) (deg)	(deg)	Filter	Obs. Year	P.A. (°)	$\rho * \sigma_\theta$ (mas)	Sep. (″)	σ_{sep} (mas)	Delta Mag. (mag)	Min. Sep. (″)	Limiting Δm 0.″15	1″
695	55559618	73.13838	-64.92922	I	2019.534						0.064	2.65	4.31
697	77253676	69.70413	-36.68003	I	2019.537	138.2	1.5	1.160	1.8	4.9	0.064	2.36	4.63
697	77253676	69.70413	-36.68003	I	2019.537	165.9	1.6	0.071	0.6	0.2	0.064	2.36	4.63
699	149302744	83.38228	-62.10936	I	2019.537						0.064	2.62	4.73
701	219239945	64.52142	-53.80139	I	2019.534						0.064	2.57	4.52
702	237914496	56.17512	-65.19892	I	2019.534						0.076	2.16	3.75
703	237928815	57.99963	-59.88256	I	2019.534	221.8	2.6	1.415	2.6	4.7	0.064	2.71	4.69
706	219345200	74.75233	-49.73608	I	2019.537						0.064	2.60	4.95
708	391821647	82.76480	-70.35725	I	2019.614						0.064	2.68	4.10
711	38510224	62.51608	-61.94253	I	2019.534						0.069	2.42	3.98
720	131419878	118.03725	-37.79850	I	2019.377						0.041	3.21	5.59
721	38571020	63.19922	-64.34764	I	2019.534						0.064	2.54	4.62
729	144138509	176.03555	-9.94889	I	2019.533						0.064	2.45	4.49
733	106402532	159.40922	-40.88833	I	2019.533						0.064	2.60	4.78
740	310009611	152.11830	-50.30730	I	2019.533						0.064	2.73	4.49
745	444842193	147.75747	-55.31856	I	2019.533						0.064	2.71	4.23
754	72985822	189.29717	-42.41333	I	2019.533						0.068	2.21	3.74
755	73228647	190.03660	-44.31198	I	2019.533						0.064	2.45	4.80
756	73649615	192.10472	-45.47056	I	2019.533						0.075	2.20	3.53
757	130924120	187.99467	-35.55481	I	2019.533						0.064	2.39	4.84
758	131081852	189.76197	-31.99247	I	2019.533	349.0	0.5	0.174	0.8	1.1	0.064	2.07	4.49
759	152147232	169.90962	-39.46211	I	2019.533	234.6	3.1	2.694	3.1	3.6	0.064	2.18	3.99
760	162362398	169.41445	-44.01711	I	2019.533						0.066	2.30	3.91
761	165317334	179.26345	-38.10472	I	2019.533						0.064	2.28	4.68
763	178819686	194.46815	-39.75833	I	2019.533						0.064	2.41	4.83
764	181159386	174.30288	-38.30719	I	2019.533						0.064	2.31	4.10
765	219401954	78.16509	-53.74353	I	2019.537						0.064	2.36	4.90
768	229811538	198.63567	-24.14419	I	2019.533						0.070	2.15	3.71
771	277634430	164.11345	-72.98547	I	2019.533						0.087	2.25	2.94
772	286864983	190.19150	-21.87275	I	2019.533	165.3	8.3	2.342	8.3	5.8	0.064	2.44	4.33
775	304042899	164.80012	-59.23375	I	2019.533						0.064	2.73	4.55
777	334305570	183.11878	-49.00739	I	2019.533						0.064	2.52	4.71
778	335630746	199.33404	-15.27361	I	2019.533						0.064	2.39	4.65
779	374095457	159.93309	-48.99672	I	2019.533	165.3	2.0	1.538	2.2	4.8	0.064	2.48	4.64
782	429358906	183.92091	-18.91022	I	2019.533						0.065	2.19	4.03

Table 5 – *Continued*

TOI	TIC	R.A., Dec. (J2000) (deg)	(deg)	Filter	Obs. Year	P.A. (°)	$\rho * \sigma_\theta$ (mas)	Sep. (″)	σ_{sep} (mas)	Delta Mag. (mag)	Min. Sep. (″)	Limiting Δm 0.″15	1″
783	451645081	172.15573	-54.78367	I	2019.533						0.064	2.48	4.50
784	460984940	159.34120	-63.65603	I	2019.533						0.064	2.71	4.43
785	374829238	88.33742	-65.63356	I	2019.614						0.066	2.66	4.03
787	350584963	87.11559	-56.00414	I	2019.537						0.064	2.38	4.74
792	294780517	71.24583	-67.98111	I	2019.534						0.068	2.32	3.91
796	277099925	83.98655	-67.45958	I	2019.614						0.067	2.51	3.88
800	179308757	79.76587	-69.63792	I	2019.614						0.072	1.99	3.35
807	30853470	75.91554	-66.65508	I	2019.534						0.064	2.55	4.03
809	149301575	82.97946	-60.47703	I	2019.537						0.064	2.57	4.85
810	388106759	62.85417	-69.47492	I	2019.534						0.064	2.70	4.40
811	100757807	88.03053	-32.92517	I	2019.614						0.064	2.32	4.44
812	363914762	89.23566	-49.00694	I	2019.614						0.064	2.48	4.49
813	55525572	72.69403	-60.90544	I	2019.534						0.064	2.64	4.54
815	102840239	155.87192	-43.83494	I	2019.533						0.064	2.64	4.85
816	175180796	116.01073	-36.99647	I	2019.377						0.041	2.70	4.83
817	30312676	74.28680	-66.39033	I	2019.534						0.069	2.54	3.99
821	125405602	209.61570	-23.27761	I	2019.613						0.067	2.32	4.04
823	158978373	218.65825	-40.74011	I	2019.533						0.064	2.27	4.35
824	193641523	222.16580	-57.58783	I	2019.533						0.052	2.38	4.09
829	276128561	224.20810	-37.04236	I	2019.534						0.064	2.31	4.41
831	307610438	229.03346	-38.87531	I	2019.533	327.9	0.4	0.167	0.1	1.4	0.064	2.13	3.55
832	350332997	84.08154	-54.19119	I	2019.614	63.9	5.9	3.213	5.7	4.7	0.064	2.52	4.07
833	362249359	145.65942	-62.48406	I	2019.533						0.064	2.90	4.19
835	405700729	192.05766	-56.89428	I	2019.533						0.066	2.67	4.31
836	440887364	225.08136	-24.45401	I	2019.533						0.064	2.22	3.48
837	460205581	157.03742	-64.50525	I	2019.533	281.7	3.6	2.313	3.6	4.6	0.064	2.74	4.27
838	461271719	203.16663	-38.84594	I	2019.533						0.064	2.63	4.99
840	287563610	198.13375	-45.59056	I	2019.533						0.079	2.19	3.54
844	380886535	19.46103	0.34667	I	2019.613						0.070	2.35	3.59
845	32283946	24.17267	-31.67081	I	2019.613						0.064	2.21	4.17
846	229141709	26.37620	-51.29658	I	2019.613						0.064	2.66	4.19
847	231289421	43.87533	-53.66519	I	2019.614	317.1	0.2	1.245	0.2	0.7	0.066	2.58	3.67
848	42015200	24.21600	-39.14256	I	2019.613						0.064	2.51	4.24
849	33595516	28.71553	-29.42178	I	2019.613						0.064	2.29	4.19
850	423670610	9.76587	-17.22178	I	2019.613						0.064	2.42	4.37

Table 5 – *Continued*

TOI	TIC	R.A., Dec. (J2000) (deg)	(deg)	Filter	Obs. Year	P.A. (°)	$\rho * \sigma_\theta$ (mas)	Sep. (″)	σ_{sep} (mas)	Delta Mag. (mag)	Min. Sep. (″)	Limiting Δm 0.″15	1″
851	40083958	7.38741	-10.46844	I	2019.613	253.8	4.9	1.858	4.9	5.2	0.064	2.39	4.23
852	29918916	24.74025	-7.28092	I	2019.613						0.064	2.31	4.14
853	138727432	32.91425	-37.89294	I	2019.613						0.064	2.63	4.57
854	160222069	28.07770	-43.04758	I	2019.613						0.064	2.54	4.38
855	269558487	15.54295	-2.14481	I	2019.613						0.064	2.53	4.09
856	306338882	14.09492	-14.78833	I	2019.613						0.064	2.39	4.13
857	404467699	25.87130	-14.14917	I	2019.613						0.064	2.27	4.30
858	198008005	60.19975	-54.59289	I	2019.614						0.064	2.86	4.61
860	321011127	43.54617	-41.51453	I	2019.614						0.064	2.68	4.55
864	231728511	81.44372	-51.35706	I	2019.614						0.064	2.62	4.46
865	44797824	62.45447	-26.02200	I	2019.614						0.064	2.55	4.67
866	381976956	77.54694	-57.58667	I	2019.614						0.064	2.91	4.57
869	200807066	53.17785	-51.78928	I	2019.614						0.064	3.04	4.79
870	219229644	63.31875	-50.94442	I	2019.614						0.064	2.91	4.82
871	219344917	74.73804	-50.62703	I	2019.614						0.064	2.57	4.83
872	220459826	74.86809	-55.92917	I	2019.614						0.066	2.68	4.20
875	14165625	78.03712	-37.70836	I	2019.614						0.064	2.47	4.19
878	219380235	76.76166	-51.76703	I	2019.614						0.064	2.74	4.43
900	210873792	245.90545	-31.37319	I	2019.613						0.064	2.20	4.10
901	214361331	261.06315	-50.38625	I	2019.613						0.064	2.65	4.10
902	216935214	259.49575	-45.88367	I	2019.613						0.064	2.44	4.61
905	261867566	227.65892	-71.36150	I	2019.613	100.8	11.1	2.276	11.1	5.9	0.072	2.37	3.53
906	298372701	239.82571	-49.36650	I	2019.613	50.8	0.3	1.246	0.3	2.8	0.064	2.94	4.61
907	305424003	262.18425	-62.84025	I	2019.613	52.0	0.9	3.667	1.0	1.1	0.063	2.84	5.12
909	364107753	251.36163	-71.83994	I	2018.255	267.6	1.2	1.344	1.2	4.1	0.041	1.49	3.59
912	406941612	229.33720	-80.47306	I	2019.613						0.065	2.43	3.27
913	407126408	234.57367	-80.80314	I	2019.613						0.064	2.59	3.40
914	153027658	48.72625	-44.96178	I	2019.614	171.3	0.4	0.104	0.1	0.1	0.064	2.07	4.35
915	259389219	68.80383	-51.39656	I	2019.614						0.064	2.82	4.72
917	207237016	49.81638	-59.40014	I	2019.614						0.064	2.78	4.63
918	294869729	71.79921	-68.98567	I	2019.614						0.066	2.51	3.88
923	301051430	50.03620	-45.06189	I	2019.614						0.064	2.59	4.50
924	382068562	79.65665	-55.88872	I	2019.614						0.066	2.77	4.38
926	176796997	48.37875	-32.00553	I	2019.614	159.6	1.0	0.190	0.3	2.2	0.064	2.10	4.53
929	175532955	45.90628	-39.93092	I	2019.614						0.064	2.51	4.56

Table 5 – *Continued*

TOI	TIC	R.A., Dec. (J2000) (deg)	(deg)	Filter	Obs. Year	P.A. (°)	$\rho * \sigma_\theta$ (mas)	Sep. (″)	σ_{sep} (mas)	Delta Mag. (mag)	Min. Sep. (″)	Limiting Δm 0.″15	1″
930	100921768	54.30875	-44.47206	I	2019.614	32.6	0.4	0.692	0.9	2.5	0.064	2.68	4.42
931	206474443	57.33684	-47.91817	I	2019.614	56.8	1.4	0.112	1.6	0.3	0.068	1.94	3.80
938	332660150	63.03237	-12.11881	I	2019.614						0.064	2.55	4.29
939	67772767	63.78697	-7.31542	I	2019.619						0.124	1.62	2.31
945	167714792	80.45533	-36.67383	I	2019.614						0.064	2.51	4.43
952	319312479	61.77947	-13.76689	I	2019.614	59.4	0.3	0.118	8.3	3.6	0.064	2.36	4.62
952	319312479	61.77947	-13.76689	I	2019.614	135.0	0.8	1.168	0.7	4.7	0.064	2.36	4.62
954	44792534	61.94117	-25.20875	I	2019.614	50.2	7.5	2.347	7.5	6.2	0.064	2.46	4.71
955	146467675	76.08187	-20.73197	I	2019.619						0.126	1.65	2.50
956	146434840	75.36047	-22.38208	I	2019.619						0.124	1.62	2.43
1024	141482386	86.82043	-72.42264	I	2019.614						0.064	3.01	4.18
1029	374908020	88.73923	-65.96029	I	2019.614						0.064	3.07	4.48
1033	149601557	87.28250	-60.49850	I	2019.614	220.4	0.6	0.268	0.2	1.7	0.064	2.84	4.47
1049	16288184	253.76888	-28.71056	I	2019.613	154.2	10.4	1.278	10.4	5.6	0.064	2.27	4.03
					Community TOIs								
	100103200	24.68040	-45.24189	I	2019.534						0.064	2.53	4.52
	141712167	90.88167	-72.76458	I	2019.199	296.5	0.4	1.418	1.2	1.6	0.068	2.62	4.10
	166527623	207.52626	-40.83575	I	2019.533						0.044	2.68	4.88
	160708862	227.27034	-42.70497	I	2019.613	311.2	18.2	2.410	18.2	7.1	0.044	2.36	4.64
	219406747	78.81024	-53.09303	I	2019.204						0.064	3.10	4.71
	220408612	70.47625	-58.02073	I	2019.534						0.064	2.77	4.68
	234503282	11.59554	-63.47278	I	2019.534	44.4	2.8	0.526	2.3	3.1	0.068	2.11	3.63
	234504626	11.94047	-62.42314	I	2019.534				1.4	1.8	0.070	2.10	3.29
	260985864	76.63612	-80.76825	I	2018.732						0.053	2.49	3.57
	299780329	37.53012	-79.75653	I	2019.534						0.070	2.35	3.92
	293689267	97.96300	-43.53403	I	2019.377	219.2	0.1	3.262	2.2	1.5	0.041	2.33	5.17
	296859112	158.34633	-15.30928	I	2019.533						0.115	1.66	2.39
	296940429	158.89828	-15.42614	I	2019.533						0.075	2.43	3.44
	32488117	4.65492	-12.20178	I	2019.534						0.064	2.06	3.29
	388128308	63.72767	-70.49456	I	2019.534						0.068	2.19	3.71
	389669796	86.89929	-69.36656	I	2019.204						0.109	2.05	2.81
	394340319	39.36550	-79.82303	I	2019.534						0.064	2.38	3.99
	441056702	359.51892	-15.06614	I	2019.534						0.064	2.22	4.17

Note. – Columns (1) and (2) give the TOI and TIC numbers, respectively. The equatorial coordinates for J2000, in degrees, are given in columns (3) and (4). Column (5) give the filter (mostly I, with a few targets observed also in V), column (6) the date of the observation (in Julian years). For resolved binaries, columns (7) and (9) give the position angle θ and the separation ρ, while columns (8) and (10) contain estimates of

the measurement errors in tangential ($\rho\sigma_\theta$) and radial (σ_ρ) directions, in mas. The measured magnitude difference Δm is given on column (11). Some targets have multiple measurements. For unresolved sources (single stars), the columns (7) to (11) are empty. The estimated resolution limit is listed in column (12) for all stars; columns (13) and (14) give the estimated maximum detectable Δm at separations of $0.''15$ and $1''$.